A structural study of size-dependent lattice variation: In situ X-ray diffraction of the growth of goethite nanoparticles from 2-line ferrihydrite

Peter J. Heaney[1*], Matthew J. Oxman[1], and Si Athena Chen[1]

[1]Department of Geosciences, Penn State University, University Park, PA 16802

*Corresponding author: pjheaney@psu.edu; 814-865-6821

Keywords: Goethite; 2-line Ferrihydrite; Nanoparticle research; Time-resolved X-ray diffraction; Kinetics

Submitted to the *American Mineralogist*

ABSTRACT

Unlike most native metals, the unit cells of metal oxides tend to expand when crystallite sizes approach the nanoscale. Here we review different models that account for this behavior, and we present structural analyses for goethite (α-FeOOH) crystallites from ~10 to ~30 nm. The goethite was investigated during continuous particle growth via the hydrothermal transformation of 2-line ferrihydrite at pH 13.6 at 80, 90, and 100 °C using time-resolved, angle-dispersive synchrotron X-ray diffraction. Ferrihydrite gels were injected into polyimide capillaries with low background scattering, increasing the sensitivity for detecting diffraction from goethite nanocrystals that nucleated upon heating. Rietveld analysis enabled high-resolution extraction of crystallographic and kinetic data. Crystallite sizes for goethite increased with time at similar rates for all temperatures.

With increasing crystallite size, goethite unit-cell volumes decreased, primarily as a result of contraction along the *c*-axis, the direction of closest-packing (Space Group *Pnma*). We introduce the coefficient of nanoscale contraction (CNC) as an analog to the coefficient of thermal expansion (CTE) to compare the dependence of lattice strain on crystallite size for goethite and other metal oxides, and we argue that nanoscale-induced crystallographic expansion is quantitatively similar to that produced when goethite is heated. In addition, our first-order kinetic model based on the Johnson-Mehl-Avrami-Kolmogorov (JMAK) equation yielded an activation energy for the transformation of ferrihydrite to goethite of 72.74 ± 0.2 kJ/mol, below reported values for hematite nucleation and growth.

INTRODUCTION

Over the last several decades, Earth scientists have documented that nanoparticles can control the aqueous geochemistry of surficial environments due to their enhanced reactivity and their catalytic proficiency (reviewed in Hochella et al. 2008 and Sharma et al. 2015). Traditionally, the amplified role of nanocrystals is attributed to their high ratios of reactive surface area to volume. In addition to their high surficial interfaces, however, nanocrystals may react more readily than their macroscopic counterparts because of structural changes arising from their sub-micrometer dimensionality. Variations in unit-cell dimension strongly influence electronic band structure, leading to disparities in the chemical behaviors of nano- and macro- particles (Solliard and Flueli 1985; Ayyub et al. 1995).

Nearly a century ago, Lennard-Jones and Dent (1928) theorized that lattice parameters of crystal surfaces will differ from those of the bulk, and by extension Lennard-Jones (1930) argued that nanoparticles dominated by surface structure will deviate in a predictable fashion from bulk materials. Specifically, he suggested that the unit-cells of "non-ionic" compounds should increase with decreasing particle size, whereas ionic crystals will behave in the opposite fashion. Some early X-ray (Randall and Rooksby 1932) and electron (Finch and Wilman 1934; Pickup 1936) diffraction experiments offered support for a dependence of lattice parameters on crystallite dimensions. Because of the small magnitudes of variation, however, these early studies offered contrasting interpretations for the effects of particle size on unit-cell dimensions (Boswell 1951).

Models of size-induced lattice variations

Modern investigative techniques offer much higher precision for the measurement of lattice parameters, and these issues have been revisited over the past two decades. In reviewing this recent work, Diehm et al. (2012) offer three generalizations regarding size-dependent lattice variations in nanoparticles:

1) Metals and ionic crystals behave oppositely. Whereas the lattice parameters of noble metals tend to *contract* with decreasing particle size (Wasserman and Vermaak, 1970, 1972), the unit cells of most metal oxides (e.g., MgO, Fe_2O_3, Fe_3O_4, $MnCr_2O_4$) *expand* as particles become smaller (Cimino et al. 1966; Bhowmik et al. 2006; Rodenbough et al. 2017). It should be noted, however, that the unit cells of Ni (Rellinghaus et al. 2001; Duan and Li 2004) and Fe (Choi et al. 2002) nanoparticles disobey this trend. Nanocrystals of these metals expand with smaller sizes, apparently due to oxide surface layers.

2) For non-cubic metal oxides (e.g., TiO_2-rutile, TiO_2-anatase, t-$BaTiO_3$), lattice expansion with diminishing size often is anisotropic (Tsunekawa et al. 2000; Kuznetsov et al. 2009; Ahmad and Bhattacharya 2009); and

3) Even today, reported magnitudes of lattice evolution with diminishing size often are highly variable for the same compound (e.g., CeO_2: Kossoy et al. 2006; Hailstone et al. 2009; Chen et al. 2010).

Irregularities in the measurements of lattice parameters as a function of nanoparticle size can be attributed to several factors, including diverse approaches to the preparation of nanoparticles and different techniques for particle size characterization (Baldinozzi et al. 2003; Ahmad et al. 2009). Tailoring specific

nanoparticle sizes may involve annealing dry powders for different times at high temperatures (200 to 1100 ^{o}C) (e.g., Hoshina et al. 2006; Rodenbough et al. 2017; Sharma et al. 2018) or precipitating nanoparticles in aqueous solutions at relatively low temperatures (e.g. Hailstone et al. 2009). In addition, the degree of structural relaxation of nanoparticle surfaces would be expected to vary with the ambient suspension medium for the interrogation technique. For electron diffraction, particles typically are exposed to high vacuum, whereas for X-ray diffraction, the particles may be immersed in air of varying humidity. Complicating the issue further, Sharma et al. (2018) have demonstrated that hematite (Fe_2O_3) nanoparticles actually exhibit both lattice expansion and contraction with decreasing size. When α-Fe_2O_3 particles diminish in size from 75 nm to 30 nm, both the *a* and *c* axes expand. As particle diameters decrease further from 30 nm to 15 nm, however, both unit-cell parameters sharply decrease.

In light of these complexities, no single theory accounts for the variation of metal oxides with decreasing particle size, but many models have been proposed:

1) Because of the technological importance of synthetic ceria as a catalyst (Sun et al. 2012), fluorite-type CeO_2 dominates the modern literature regarding nanoscale-induced lattice expansion in metal oxides (Tsunekawa et al. 1999; Spanier et al. 2001; Wu et al. 2004; Trovarelli and Llorca 2017). Many studies have documented that Ce^{3+}–anion vacancy defects are stabilized at the surfaces of CeO_2 nanocrystals, and the larger sizes of these defect clusters have been cited as a cause of lattice expansion (Tsunekawa et al. 1999; Deshpande et al. 2005; Chen et al. 2010). These observations imply that strains from the accumulation of point defects

113 can stimulate lattice expansion. Curiously, however, increasing concentrations of O
114 vacancies for sub-30 nm Fe_2O_3 are accompanied by a lattice *contraction* (Sharma et
115 al. 2018).

116 2) Perebeinos et al. (2002) present a "Madelung model" to account for the
117 expansion of ionic materials with decreasing particle size. They consider the total
118 Madelung energy for a nanoparticle as the sum of separate surface and volumetric
119 contributions. Within the outermost surface layer, the short-range repulsive forces
120 (as modeled through the bulk modulus) outcompete the long-range attractive
121 Coulombic forces. Lattice expansion within the surface diminishes the Madelung
122 surface energy, leading to an effective negative pressure. That in turn promotes a
123 bulk lattice expansion within the nanoparticle. This model reproduces the
124 behaviors of $BaTiO_3$ and CeO_2, though Perebeinos et al. (2002) also invoke point
125 defects to account for "missing" expansion in ceria.

126 3) Fukuhara (2003) argues that lattice expansion in metal oxide
127 nanoparticles occurs because of a neutralization of the screening by inner shell
128 electrons between atomic nuclei and valence shell electrons. That occurs when the
129 proportion of free electrons from the valence shells of unbonded surface atoms are
130 replaced by inner shell electrons, effectively increasing the ionic radii and leading to
131 lattice expansion. Fukuhara (2003) invokes a Thomas-Fermi statistical method to
132 model the decrease in charge screening and increase in unit-cell volume for MgO,
133 Fe_2O_3, and TiC.

134 4) Diehm et al. (2012) focus instead on surface stresses as the driving
135 constraint for size-dependent lattice expansion. Unlike metal oxides, noble metals

contract with decreasing particle size because the metal atoms at the particle surface are under-coordinated (Mays et al. 1968), thereby increasing the residual bond strengths to the surrounding metal atoms. That generates a positive surface stress, which in turn leads to compressive tension in metals, akin to an elastic membrane enveloping the metal particle. With decreasing particle size, the surface-to-volume ratio increases, and the stress increasingly squeezes the structure.

Diehm et al. (2012) argue that, in contrast, the surface tensions of metal oxides are determined by local ionic interactions, and they will vary with planar orientation in a symmetry-dependent fashion. Diehm et al. (2012) employ density functional theory (DFT) to calculate energies and stresses of specific surface planes, arguing that their approach successfully predicts the lattice-versus-size behaviors for a host of nanocrystalline oxides.

Structural evolution of nanocrystalline goethite

Despite the many conflicting interpretations of size-dependent lattice expansion in metal oxides, few investigators offer a high-resolution crystallographic investigation of atomic structure as nanoparticles change in size. Here, we present a detailed study of the structural evolution of goethite (α-FeOOH) nanoparticles based on in situ, time-resolved synchrotron X-ray diffraction (TRXRD) during precipitation from precursor 2-line ferrihydrite ($Fe_{8.2}O_{8.5}(OH)_{7.4} \cdot 3H_2O$). Goethite is an extremely common soil mineral in wet and oxidizing environments on the Earth's surface (Kämpf and Schwertmann 1983; Hyland et al. 2015). In near-surface terrestrial settings, goethite typically forms via dissolution and recrystallization of ferrihydrite,

a poorly ordered Fe oxyhydroxide common in acid mine drainage environments (Ferris et al. 1989; Carlson et al. 2002; Michel et al. 2010). Goethite habits range from stubby nanocrystals to >1 μm-long fibers with high, reactive surface areas (Ardizzone and Formaro 1985; Blesa and Matijević 1989; Penn et al. 2006). The chemical reactivity of goethite nanocrystals depends strongly on particle size, shape and crystallinity (Waychunas et al. 2005; Gilbert et al. 2007; Stemig et al 2014).

In order to ensure that our samples were not intergrown with hematite, we investigated the growth of goethite nanoparticles from 2-line ferrihydrite gels at pH 13.6 between 80 and 100 °C. When temperatures are between 25 and 100 °C, hematite is the dominant transformation product from ferrihydrite at pH 2 to 10 (Johnston and Lewis 1983; Schwertmann et al. 2004; Das et al. 2011; Soltis et al. 2016). Goethite and hematite initially co-precipitate at temperatures between 50 and 130 °C from pH 6 to 10. After a week of hydrothermal treatment at these conditions, goethite dissolves and hematite precipitates (Das et al. 2011; Chen et al. 2018). Thus, hydrothermal synthesis of phase-pure goethite typically is achieved using highly alkaline solutions (pH > 11) and temperatures at or below 100 °C (Cornell and Giovanoli 1985; Cornell and Schwertmann 2003).

Characterizing lattice-parameter variations during crystal growth by in situ TRXRD offers several advantages over measurements of polydisperse dry powders. The high time resolution for the collection of diffraction rings (<60 s per pattern) enabled a nearly continuous monitoring of particle size. The immersion medium ensured a constant ambient environment for particle surfaces, and, its high pH notwithstanding, the aqueous fluid modeled the kinds of hydrous geochemical

systems in which goethite precipitates. Rietveld analysis of whole-ring patterns obtained by synchrotron radiation remains the most accurate method for ascertaining lattice parameters. Because we utilized an environmental cell with low background scattering of X-rays, we were able to monitor particle sizes on the order of 10 to 30 nm.

Many studies have documented similarities between the effects of shrinking nanoparticle size and increasing temperature with respect to lattice parameters and phase transitions (e.g., Ayyub et al. 1988, 1995; Quadri et al. 1999; Tsunekawa et al. 2000; Choi et al. 2002; Baldinozzi et al. 2003; Rivest et al. 2011). Here we compare structural variations in bond lengths and angles during goethite nanoparticle growth with those that accompany thermal changes in bulk goethite, as determined by the high-resolution crystallographic study of heated goethite by Gualtieri and Venturelli (1999). In addition, by measuring goethite growth at three temperatures, we were able to extract reaction rates and activation energies for goethite nucleation and growth.

EXPERIMENTAL METHODS

Sample preparation

Ferrihydrite and goethite were prepared using the method described by Schwertmann and Cornell (2000). In this study, we dissolved 0.505 g $Fe(NO_3)_3 \bullet 9 H_2O$ in 1.25 mL DI water to produce a 1 M solution of $Fe(NO_3)_3$. This solution was mixed with 2.25 mL of 5 M KOH, and 21.5 mL of DI water was added to the solution to yield 25 mL. Reddish-brown 2-line ferrihydrite, as identified by synchrotron X-

ray diffraction (see below), precipitated as a gel immediately upon the combination of the $Fe(NO_3)_3$ and KOH. The pH of the final solution was 13.6. Goethite diffraction peaks were detected in this ferrihydrite gel at room temperature after a few hours. Consequently, we developed a protocol for injection of the ferrihydrite gel into the environmental cell, followed by cell sealing and sample mounting, in less than 15 min of mixing the gel.

Construction of the environmental cell

The quartz glass capillaries that have previously served as reaction cells for TRXRD hydrothermal growth studies (Norby 1996; Parise et al. 2000; Hummer et al. 2012; Peterson et al. 2016) contribute high background scattering from amorphous silica. Therefore, for these experiments we modified the Norby-type environmental cell to test the applicability of polyimide (Kapton®) for fluid containment, since polyimide exhibits a higher transmittance of X-rays than does quartz glass. The resultant increase in sensitivity of X-ray detection allowed for the detection of particles measuring tens of nm. The rapid kinetics of goethite crystallization allowed us to perform hydrothermal synchrotron-based TRXRD experiments at relatively low temperatures, between 80 and 100 °C. The attendant low vapor pressures in turn enabled the testing of polyimide (Kapton®) to contain the heated ferrihydrite gels. As an organic polymer, polyimide generates a lower background than does silica, and it was chemically inert with respect to the ferrihydrite gel. We purchased polyimide tubing from Cole-Parmer (Part# 95820-06), with dimensions 0.0320" ID x 0.0340" OD (0.813 mm ID x 0.864 mm OD) and thus a wall thickness of 0.0020" ±

0.0005" (50.8 μm ± 12.7 μm). Attempts to heat the gels above 100 °C consistently yielded vapor release ruptures in the polyimide tubing, leading to total dehydration of the gel.

The time sensitivity of the gels to spontaneous crystallization required a method for rapid sealing of the vessels after sample loading. Initially, we attempted to seal the polyimide capillaries with a high-temperature RTV (room-temperature vulcanization) silicone sealant (Loctite®). Although this sealant does not fully cure until 24 hr after application, it is tack-free after only 30 min and stable up to 315 °C. However, the silicone adhesive did not adhere adequately to the polyimide surfaces. When the cell temperatures attained 100 °C, the solution pressure ejected the silicone plug (and the reaction mixture) from the tube. Instead, we achieved success with a commercial 5-minute epoxy (Devcon®). Although the full cure time for Devcon is 1 hr, this epoxy dried sufficiently for experimental use after 15 min. When capillary solutions were heated to 100 °C for 8 hr, the epoxy remained sufficiently stable to contain the hydrothermal reaction mixture.

Protocol for sample preparation.

After these and other tests were completed, a consistent sample preparation method was developed. First, ferrihydrite was freshly mixed at the start of each experiment to avert the precipitation of goethite. Gel was extracted from the mixing vessel with a 1 mL syringe and then injected into a 2.5 cm length of polyimide tubing. The 5-minute epoxy then was liberally applied at both ends of the capillary to minimize any head space between the epoxy and the gel. Care was taken to

maintain the bulb of the epoxy seal to a diameter of <2 mm to allow for the insertion of the capillary into a standard brass mounting pin for loading within an X-ray goniometer. The capillary was secured within the brass pin by a small amount of clay. The experimental design is shown in Figure 1.

Synchrotron X-ray diffraction

In situ time-resolved X-ray diffraction experiments were conducted at the GeoSoilEnviroCARS (GSECARS) Beamline 13-BM-C at the Advanced Photon Source (APS), Argonne National Laboratory (ANL). The X-ray wavelength was 0.8292(8) Å, and the detector distance was 95.165 mm, as determined by refinement of a LaB_6 standard. Capillary orientation was maintained at horizontality for the duration of the experiments since tilting the capillaries resulted in a separation of the gel from the aqueous phase, inhibiting the precipitation of goethite. The beam measured approximately 0.3 mm in height and 0.4 mm in width, and it was directed towards the middle of the capillary both horizontally and vertically. We observed that the ferrihydrite gels gravitationally separated slightly from the aqueous solutions towards the bottom half of the capillary, but enough material remained within the X-ray window to ensure high-quality diffraction patterns. Capillaries were rotated about phi by 1° per s to minimize preferred orientation effects in the X-ray diffraction patterns.

A forced-gas heater fabricated at APS consisted of wound Ni coils around an inner ceramic tube, with an applied DC voltage using a Sorensen 33 V x 33 A (Model XHR 33-33) power supply to achieve resistive heating. This assembly was encased

in an outer ceramic sleeve, and He gas was forced through the interior of the heated cylinder. The heater was oriented normal to the capillary, and a type K chromel-alumel thermocouple was situated adjacent to the capillary. The current was monitored with a Keithly 2700 Multimeter. The thermocouple had been previously calibrated by monitoring two phase transformations of $RbNO_3$ (Alfa Aesar, 99.8%, metals basis) loaded in a 1.0 mm quartz glass capillary and heated from 25.7 to 250 °C. Based on this standardization, we estimate that the temperature measured by the thermocouple was within ± 1.5 °C of the actual temperature.

Experiments were run until reactions had apparently ceased; at 80, 90, and 100 °C, the run times were 8, 7, and 2 hours respectively. Individual diffraction patterns were collected for 50, 40, and 40 seconds, respectively, using a MAR165 CCD camera with no wait time between data collections. Experimental temperatures were attained by the start of the second pattern using a proportional-integral-derivative (PID) controller. Patterns were collected until XRD peak intensities registered no measurable increase. Full-circle images were integrated into linear intensity-versus-2θ datasets using the program Dioptas (Prescher and Prakapenka, 2015).

Structure refinement

Rietveld structure refinements were performed using the EXPGUI interface of the General Structures Analysis System (GSAS) program (Larson and Von Dreele 2004; Toby 2001). The initial goethite structure parameters (S.G. *Pnma*) were taken from Szytuła et al. (1968). Initially, unit-cell parameters, scale, sample displacement, and background were allowed to refine. The Gaussian peak shape coefficients *GU*, *GV*, and *GW* were fixed at 0.0, -13.52, and 10.38, respectively, as determined by refinement of a LaB_6 standard analyzed at the start of our data collection. Backgrounds were best fit for all patterns using a shifted Chebyschev polynomial with 12 to 21 terms. Peak profiles were modeled using a pseudo-Voigt function described by Thompson et al. (1987).

The profile parameters for Lorentzian broadening (*LX*) and anisotropic Lorentzian broadening (*ptec*) were refined. After these parameters converged the atomic positions for both O atoms and Fe were refined. Iron occupancy was refined but did not deviate from unity for any patterns. The refinement of isotropic temperature factors (U_{iso}) generated negative values, and therefore in all refinements, values for U_{iso} were fixed to 0.005 for Fe and O. Refinements were performed over a 2θ range from 15.500° to 36.203° (d-spacings of 3.0708 Å – 1.3344 Å). Low-angle data were not included in the refinement because of the large background scattering from water. The total number of patterns analyzed for 80, 90, and 100 °C experiments were 35, 33, and 24 respectively, representing time-sampling intervals ranging from 2 to 10 min. Goodness-of-fit parameters indicated

high-quality refinements, with χ^2 ranging from 0.03 to 0.40, R_{wp} from 0.001 to 0.004, and R_{Bragg} from 0.010 to 0.030.

Particle size determination

Mean particle sizes were calculated for all three experiments using multiple methods. We applied a "manual Scherrer" method via the Scherrer (1918) formula:

$$\tau = \frac{K\lambda}{\beta cos\theta} \quad (1)$$

where τ is the mean particle size, K is the crystal shape factor (in this case 1), β is the full width at half maximum (corrected for instrumental broadening), and θ is the Bragg angle. In order to account for instrumental broadening, the full-width at half-maximum (FWHM) of the (110) diffraction peak of a LaB_6 standard was measured using Jade2010 software (Materials Data, Inc.), and that value was subtracted from the FWHM of the (101) diffraction peak of the emergent goethite. Secondly, since instrumental broadening was compensated through the Cagliotti coefficients (*GU*, *GV*, *GW*) refined for a LaB_6 standard, we also calculated particle sizes from the refined Lorentzian isotropic broadening parameter (*LX*):

$$\tau = \frac{18000 \cdot K\lambda}{\pi \cdot LX} \quad (2)$$

where K is the Scherrer constant (=1) and λ is the wavelength (Larson and von Dreele 2004). "Manual Scherrer" analysis using the (101) goethite peak and whole pattern Rietveld refinement agreed to within 5% for diameters >15 nm. For particles <15 nm, Rietveld methods proved more internally consistent than manual Scherrer analysis.

In order to compare crystallite size-dependent changes in the unit-cell volumes of other materials relative to goethite, graphical data published in other articles were digitized by WebPlotDigitizer 4.2 when values were not explicitly tabulated in the reports.

Scanning and transmission electron microscopy

Goethite was grown from ferrihydrite gels in quartz glass capillaries under identical conditions as characterized our in situ TRXRD experiments. Capillaries then were broken open to allow analysis of the contents by scanning electron (SEM) and transmission electron microscopy (TEM). For SEM analysis, samples were placed on double-sided sticky C tape and imaged using a Scios SEM at 3 keV and 50 pA. For TEM analysis, reaction products were prepared by ultrasonicating a small amount of the goethite in ethanol, then air drying on a holey C film supported by a copper-mesh TEM grid. TEM images were obtained using an FEI Talos F200X (S)TEM at 200 kV.

Kinetic modeling

We calculated the initial rate constants using the Johnson-Mehl-Avrami-Kolmogorov equation (JMAK):

$$\alpha = 1 - e^{-[k(t-t_o)]^n} \quad (3)$$

where α represents reaction progress, k is the rate constant (s^{-1}); t is time elapsed (s); t_o is the induction time representing the time lapse from the start of data collection until the onset of crystallization (s), and n is the reaction order (Avrami

1939 and 1940; Johnson and Mehl 1939). In these experiments, goethite peaks were apparent as soon as the target temperature was achieved (i.e., the second diffraction pattern in each temperature series). Consequently the induction time t_o for crystallization at 80, 90, and 100 °C was effectively zero. The value for reaction progress α was calculated for a specific temperature by normalizing the scale factor S_{ph} at a given time to the maximum scale factor at that temperature, as represented by the final diffraction pattern in a temperature series ($S_{ph}/S_{ph(max)}$). Our data were well fit by a first-order reaction model, consistent with the goethite crystallization experiments of Shaw et al. (2005).

These considerations simplified the JMAK equation to:

$$\alpha = 1 - e^{-kt} \quad (4)$$

Using the Igor Pro 8 software (Wave Metrics), we refined the rate constant, k, to achieve the best fit to Equation (4) at each temperature. The calculated rate constants were then used to calculate the activation energy with the Arrhenius equation:

$$\ln(k) = \ln(A) - \frac{E_a}{R}\left(\frac{1}{T}\right) \quad (5)$$

where k is the rate constant (s^{-1}), A is the pre-exponential factor (s^{-1}), E_a is the activation energy (J/mol), R is the gas constant (8.31446 J/mol•K), and T is temperature (K). E_a was extracted from this relationship by plotting the natural log of the three rate constants as a function of $1/T$. The resulting slope was multiplied by the gas constant to determine the activation energy.

RESULTS

Crystallite versus particle size

Crystallite size based on XRD Scherrer analysis yields the average dimension of coherently diffracting domains, which can be orders of magnitude different from particle sizes (Holzwarth and Gibson 2011). Our SEM and TEM investigation of goethite samples synthesized in parallel with the TRXRD experiments revealed lathlike particles that measured up to 5 μm in length and 300 nm in width (Fig. 2a). Even at low magnifications, high defect densities were apparent, and higher magnifications clearly showed that these micrometer-long laths are aggregates of slightly-to-strongly misaligned crystallites that measure tens of nm in dimension (Fig. 2b). Fast Fourier transforms of high-resolution TEM images revealed that the μm-long fibers were elongate along the *b*-axis, which is the tunnel direction in the *Pnma* setting for goethite. Extremely high densities of stacking faults were apparent normal to *b* along the (001) planes, reflecting the direction of O closest-packing in goethite. Thus, the fibers evidently grew through attachment of nanocrystals along *b*, followed by side-by-side fiber aggregation along *c*.

Nanocrystalline sub-structures were expected in light of the many studies demonstrating growth of goethite via oriented aggregation of nanocrystals (Guyodo et al. 2003; Burleson and Penn 2006). Likewise, Sharma et al. (2018) differentiate between crystallite sizes that measure in the tens of nanometers versus particle sizes up to 1 μm in diameter in their examination of nanoscale-induced lattice variations in hematite. In instances when nanoparticles actually consist of single nanocrystals, the Scherrer-based analysis that we employed in the present study

yielded very close agreement with sizes ascertained using TEM (e.g., Borchert et al. 2005; Rodenbough et al. 2017).

The crystallite sizes detected by our XRD analysis also are consistent with those reported in previous studies for nearly identical synthesis conditions. For example, Schwertmann et al. (1985) calculated the size of goethite crystallites by Scherrer analysis for synthesis from ferrihydrite gels at 80 °C. Their nanocrystals attained a size of 38 nm, slightly larger than the dimension of 28 nm calculated in the present study at 80 °C. We attribute this discrepancy to different durations of the experiments, since Schwertmann et al. (1985) conducted their 80 °C experiment for 7 days, whereas ours ran only for 6.3 hr. Although Rietveld analysis yields only a single averaged crystallite diameter, the small size regime for our nanocrystals renders these values reasonably close to actual dimensions.

Evolution in goethite crystallite size

For all goethite synthesis temperatures, the first few diffraction patterns (Fig. 3) revealed only two broad, low-intensity peaks arising from 2-line ferrihydrite, at 22° 2θ and 32° 2θ (2.17 and 1.50 Å). Despite the high background contributed by the polyimide tubing and the aqueous phase in the ferrihydrite gel, diffraction peaks corresponding to emergent goethite were discernible in the second pattern of each series, indicating precipitation just as the target temperature was achieved within 40 s. Rietveld analysis yielded reasonable fits to the diffraction patterns once the background was properly modeled, and a representative refinement for the final stages in each experiment can be seen in Figure 4.

The first particles of goethite with diffraction peaks that were sufficiently distinct from the background to enable analysis by "manual Scherrer" and Rietveld techniques were on the order of 10 nm (Fig. 5). Final crystallite sizes differed for each temperature run, ranging from 18 nm to 28 nm. This disparity may be explained by the differences in total run times, which in turn were determined by the cessation of crystal growth within the capillary windows and ranged from ~100 min at 100 °C to ~400 min at 80 °C. The change in crystal size with time was marked by two stages of linear growth – an initial interval of rapid expansion followed by a period of slower growth. When ferrihydrite was heated to 90 °C (Fig. 5), a change in growth rate occurred at 40 min.

Changes in unit-cell dimensions during goethite crystallization

Goethite mirrors most other metal oxides in its contraction of lattice parameters with increasing nanoparticle size. At 80, 90, and 100 °C, the growth of goethite nanoparticles was accompanied by a decrease in the magnitudes of *a*, *b*, and *c*, and therefore, of unit-cell volume (blue diamonds in Fig. 6). Of the three cell-edge parameters, the *c*-axis – which is normal to the plane of closest packed O atoms – exhibited the largest change, decreasing, for example, from 4.637(2) Å to 4.615(1) Å as particles increased from 9.5 nm to 18.3 nm at 90 °C. Thus, a particle diameter increase of ~9 nm was associated with a decrease of 0.47% in the *c* direction, and the unit-cell volume contracted by 0.69%.

As seen in Fig. 6, our refined unit-cell parameters (blue diamonds) differed from those of Gualtieri and Venturelli (1999-red squares) by ~0.01 to ~0.04 Å. The

452 discrepant magnitudes are attributable to the starting materials. Gualtieri and
453 Venturelli (1999) employed a synthetic sample from Bayer AG that was produced by
454 high-temperature oxidation and hydrolysis of an Fe-sulfate in the presence of
455 metallic iron, and the particles exhibited an acicular morphology with 1 μm-long
456 needles. Our preparation protocol and the sizes of our nanoparticles more closely
457 paralleled those of Szytuła et al. (1968), and the refined lattice parameters for our
458 end-product nanogoethite closely matched their reported values (green triangles in
459 Fig. 6).
460
461 **Kinetics of goethite crystallization**
462 As quantified by the refined scale factors for goethite, the rate of goethite
463 crystallization from 2-line ferrihydrite increased with temperature. At all three
464 temperatures, however, the crystallization rate decreased with time. Therefore, we
465 analyzed the kinetics of crystallization using a JMAK model that included non-linear
466 crystallization behavior (Eq. 3). The fits are shown in Fig. 7, and the rate constants
467 calculated from them are presented in Table 1. Our refined rate constants yielded χ^2
468 values ranging from 8.2×10^{-2} to 9.9×10^{-5}, indicating a high confidence in these values.
469 The natural logs of these rate constants were then plotted against 1/Temperature to
470 determine the activation energy (Fig. 8). The JMAK model yielded an E_a of 72.74 ±
471 0.2 kJ/mol. The calculated activation energies exhibited an excellent correlation
472 coefficient, with R^2 of 0.999996, evidence of the high internal consistency of our in
473 situ synchrotron hydrothermal experiments.
474

DISCUSSION

Nanoparticle size as a proxy for temperature

Similarities in the structural strains associated with nanoparticle size and changes in temperature (Ayyub 1988, 1995) and pressure (Tolbert and Alivisatos 1994) have been noted for many decades. For example, Pawlow (1909) predicted over a century ago that melting temperatures (T_m) are reduced for smaller crystallite dimensions, and a plethora of studies have documented significant decreases in T_m for both nanoparticulate metals (Takagi 1954; Koga et al. 2004; Sun and Simon 2007) and semiconductors (Goldstein et al. 1992).

Likewise, solid-state phase transitions often are shifted to lower critical temperatures (T_c) with smaller particle size (*ZnS*: Quadri et al. 1999; *$BaTiO_3$*: Tsunekawa et al. 2000, Hoshina et al. 2006, Shi et al. 2018; Panomsuwan and Manuspiya 2019; *ZrO_2*: Baldnozzi et al. 2003; *Cu_2S*: Rivest et al. 2011). This downward shift in T_c is tied to nanoscale-induced strains that drive the structures towards the higher-temperature polymorphs. For example, bulk tetragonal $BaTiO_3$ transforms to the cubic allotrope at 120 °C (Kwei et al. 1993). However, the room-temperature magnitudes of *a* and *c* for *t*-$BaTiO_3$ approach each other as nanoparticle diameters decrease, eventually achieving equality below a critical crystallite size of ~30 nm (Schlag and Eicke 1994; Hoshina et al. 2006; Panomsuwan and Manuspiya 2019), though some dispute surrounds the long-range order of the cubic nanophase (Smith et al. 2008; Shi et al. 2018). In a Landau analysis, Baldinozzi et al. (2003) similarly explore the downward renormalization of the monoclinic-tetragonal T_c of ZrO_2 as a function of particle size. They report a co-existence of the

monoclinic and tetragonal phases for particle sizes below ~60 nm, with the tetragonal volume fraction increasing to 100% at the critical diameter of 13.6 nm.

In the present study, we make an explicit comparison of the nanoscale-induced structural strains in goethite with those stimulated by temperature through reference to the high-resolution XRD heating analysis by Gualtieri and Venturelli (1999). This comparison demonstrates the considerable magnitude of nanosize-dependent lattice distortions. X-ray diffraction during in situ heating of dry goethite powders (Gualtieri and Venturelli 1999) revealed a roughly linear increase in the unit-cell volume when goethite is heated from 25 to 150 °C, with $\Delta V/V = 0.20\%$ (red squares in Fig. 6). This thermally-induced change is roughly 3.5 times less pronounced than the volume change observed as our particles grew from 9.5 Å to 18.3 Å ($\Delta V/V = -0.69\%$) (blue diamonds in Fig. 6). Deprotonation begins when goethite is heated above ~150 °C and ultimately converts to hematite, leading to a sharp contraction in the *b*-axis and an overall reversal in the thermal expansion of unit-cell volume (red squares in Fig. 6). Nevertheless, correlations of our data with lattice variations from 25 to 150 °C are structurally appropriate, and they testify to the significant influence of nano-dimensionality on crystal structure.

To compare the degree of nanoscale-induced expansion of goethite with that of other oxides, we can introduce a linear coefficient of nanoscale contraction (CNC or α_S) as an analog to the coefficient of thermal expansion (CTE):

$$\alpha_S = \frac{1}{L_b}\frac{\Delta L}{\Delta S} \quad (6)$$

where L represents a unit-cell axis dimension, and S denotes crystallite diameter (in nm). The subscript b indicates the value of L or S for the macroscopic bulk material,

This is a preprint, the final version is subject to change, of the American Mineralogist (MSA)
Cite as Authors (Year) Title. American Mineralogist, in press.
DOI: https://doi.org/10.2138/am-2020-7217

and $\Delta L = L - L_b$ and $\Delta S = S - S_b$. The units for CNC are nm^{-1}, rather than K^{-1} as with the CTE. For compounds, such as goethite, whose unit cells expand with smaller crystallite size (or contract during particle growth), α_S will be negative. Equation 6 assumes that α_S does not vary with particle size, but an examination of reported nanoscale-induced lattice variations (Supp. Info. Fig. 1) suggests that the relationship between unit-cell volume and particle size typically is non-linear. In these cases, a more precise evaluation of the CNC requires the differential form:

$$\alpha_S = \frac{1}{L_b}\left(\frac{\delta L}{\delta S}\right)_T \quad (7)$$

and integration of $\delta L/\delta S$.

The linear CNC for the *c*-axis of goethite is presented alongside those for metals and other metal oxides in Table 2. Because of the non-linearity of CNC when crystallite sizes are extended to their bulk parameters, the values in Table 2 represent secant, or mean, CNCs over crystallite size ranges that exhibit the most marked change in lattice parameters (typically between 5 and 30 nm) in a nearly linear fashion. Interestingly, the absolute magnitudes of the CNCs for metals and metal oxides generally fall within the same order of magnitude. The CNCs (in nm^{-1}) usually are 1 to 2 orders of magnitude larger than the CTEs (in K^{-1}) for the same material, again revealing that nanosize-induced strains for crystallites below ~30 nm are significant relative to thermal strains. At the same time, the overall similarity in CNCs was somewhat surprising, since the protocols for sample synthesis differed from one study to the next. The linear CNC for goethite along the *c*-axis (-5.34×10^{-4} nm^{-1}) exceeds those for Fe_2O_3 and Fe_3O_4, but is significantly smaller than that of $MnCr_2O_4$ (-9.21×10^{-4} nm^{-1}) (Table 2).

544

545 **Structural mechanism of nanoscale-induced expansion in goethite**

546 What might account for the inverse relationship between particle size and
547 unit-cell dimensions in nanogoethite? Although many studies of nano-CeO_2 have
548 identified increased concentrations of vacancies as a contributor to lattice
549 expansion (Tsunekawa et al. 1999; Deshpande et al. 2005; Chen et al. 2010), our
550 Rietveld refinements of goethite did not implicate vacancies. In this respect,
551 goethite nanoparticle evolution departs significantly from that of hematite. Our
552 group's earlier TRXRD studies of hydrothermal hematite growth (Peterson et al.
553 2015; 2018) reveal an initially high Fe vacancy concentration in the first-formed
554 nanocrystals (Fe_{occ} = ~0.70), followed by a regular increase in Fe occupancy that
555 mirrors the loss of H^+ from the structure. Unlike hematite, however, the observed
556 unit-cell changes in goethite cannot be ascribed to changes in the hydration state of
557 the solid. Our Rietveld analyses of the crystallization of goethite revealed no change
558 in Fe occupancy, as Fe_{occ} refined to unity starting with the incipient nanocrystals.
559 Similarly, Gualtieri and Venturelli (1999) note that unit-cell expansion during the
560 heating of dry goethite powders from 50 to 150 ^oC was not accompanied by a
561 change in Fe_{occ} or by the loss of protons.

562 Instead, we argue that the "Madelung-model" of Perebeinos et al. (2002)
563 captures the essence of the nanoscale behavior exhibited by goethite. As particles
564 decrease in size, the longer-range Coulombic attractions diminish in their capacity
565 as restoring forces, whereas the shorter-range repulsions become relatively more
566 significant. In this fashion, diminishing particle size should exhibit characteristics

similar to increasing thermal perturbations. If so, one might expect that the bond distances and angles as nanoparticle diameters decrease will respond in a fashion similar to an increase in temperature. In Fig. 10 of their paper, Gualtieri and Venturelli (1999) explain the thermal expansion of goethite by examining the Fe-O2 bond length, the Fe-O2-Fe bond angle between edge-sharing octahedra, and the Fe-O2-Fe bond angle between adjacent octahedra and oriented parallel to the *b*-axis. This last bond angle by symmetry is equal to the O2-Fe-O2 bond angle along *b*, and we have labeled it as such in Figure 9.

The extraction of bond information from our in situ hydrothermal XRD refinements was challenged by the high background from our environmental cell, and the analyses were particularly difficult for the earliest crystallites, since their diffraction peaks were extremely weak and broad. Consequently, our confidence in bond determinations for particles below ~14 nm in diameter is low. On the other hand, when we examined the dependence of the Fe-O2 bond length and the two bond angles with increasing particle size (Fig. 9), and compared our refined values with those observed by Gualtieri and Venturelli (1999) during heating, it was apparent that not only the trends but the absolute magnitudes of these structural parameters closely matched. In other words, the mechanistic pathway by which the goethite structure expands when heated is virtually identical to that followed during nanoscale-induced structural expansion.

Kinetic modeling

Although the conversion of goethite to hematite has been heavily studied, the transformation kinetics of ferrihydrite to goethite are less well understood. For example, several papers have reported activation energies for the transformation of goethite to hematite (Goss 1987; Walter et al. 2001; Fan et al. 2006; Murray et al. 2009) and of the dissolution of goethite in acidic solutions (Cornell et al. 1976; Sidhu et al. 1981; Cocozza et al. 2002). Kinetic studies of goethite growth from either 2-line ferrihydrite or schwertmannite, however, are sparse and have been achieved primarily by energy dispersive powder diffraction (EDPD) (Shaw et al. 2005; Yee et al. 2006; Davidson et al. 2008). Of these papers, the most germane to the present study is the EPDP analysis by Shaw et al. (2005), who examined aqueous goethite crystallization from 2-line ferrihydrite with and without phosphorus at pH 13.7.

Consistent with our results, they modeled the growth of goethite from 2-line ferrihydrite as a first-order reaction. However, the activation energy for goethite crystallization at pH 13.7 was measured as 39 kJ/mol – about half our calculated value of 73.6 kJ/mol. Due to the lower resolution of EDPD relative to the angle-dispersive, constant-wavelength protocol employed in the current study, Shaw et al. (2005) were unable to detect the onset of crystallization at the early stages that our technique allowed, nor did EDPD enable the coupling of rate data with crystallographic measurements. Consequently, Shaw et al. (2005) assumed an induction time of more than 60 seconds for all of their experimental runs, whereas we observed the appearance of goethite peaks within our second data collection, as soon as the environmental cell attained the set temperature. As is evident from Eq.

612 3, an increase in induction time in the JMAK analysis requires the inclusion of an
613 activation energy for nucleation that is distinct from the E_a for crystal growth, and it
614 results in a higher rate constant for a given degree of reaction progress, thereby
615 lowering the calculated activation energy for goethite particle growth.

616 Both the activation energies of Shaw et al. (2005) and the present study are
617 lower than those reported for hydrothermal crystallization of hematite from 2-line
618 ferrihydrite. Our analysis of the kinetic data in Das et al. (2011) yields an activation
619 energy of ~151 kJ/mol for hematite growth at pH 10, the closest match in that study
620 to our synthesis conditions. At the other end of the pH spectrum, Peterson et al.
621 (2016) employed angle-dispersive, constant wavelength TRXRD to investigate the
622 hydrothermal formation of hematite at pH ~1 from akaganeite (β-FeOOH), and their
623 JMAK analysis yielded an E_a for the nucleation and crystal growth of hematite of 80
624 ± 13 kJ/mol and 110 ± 21 kJ/mol, respectively. The lower activation energies that
625 we and Shaw et al. (2005) have calculated for goethite crystallization relative to
626 published values for hematite begin to explain the appearance of goethite in natural
627 environments, even when hematite is the stable phase.
628

629 **IMPLICATIONS**

630 As exemplified by the present study of goethite, changes in crystallite
631 diameters of a few tens of nms are comparable to temperature variations of
632 hundreds of K in terms of induced lattice strain, and these lattice strains reflect
633 underlying structural distortions that will significantly alter the physical properties
634 of minerals, including their phase stability, reactivity, and dielectric and magnetic

responses (Ayyub 1998; Diehm et al. 2012). Despite many studies of the dependence of unit-cell parameters on crystallite size over the last three decades, scientists are still debating among models that quantify variations in nanoscale-induced lattice expansion, even for simple metal oxides. This situation parallels that of the effects of point defect-induced strains on lattice parameters and phase transitions (Heaney 2000). While phenomenological approaches such as Landau analysis provide helpful descriptive tools to quantify the relationships, our capabilities for predicting the range of CNCs in Table 2 are wanting.

Although X-ray diffraction techniques cannot capture surface structures, which may ultimately control overall stability (Navrotsky 2009), the crystallite structures detected by XRD reveal that the interiors of nanoparticles are not identical to those of macroscopic crystals. Therefore, nanocrystallites can sample structural states that may not be easily accessible in macroscopic particles. For example, our refined structures for the smallest nanogoethite crystals suggest how the bulk structure might respond to increased temperature if deprotonation did not accompany heating of goethite. Moreover, core-shell models that compare surface energies of nanoparticles with volumetric energies cannot simply employ the bulk material as a proxy for nanoparticle interiors. We argue that in situ XRD analyses of the growth and dissolution of nanoparticles offer uniquely self-consistent insights to develop a deeper understanding of the relationship between lattice strain and particle size, because CNCs likely reflect a complicated interplay of strained surface and interior structures.

Acknowledgments

This work was made possible by the National Science Foundation Grants EAR1552211 and EAR1925903. GeoSoilEnviroCARS is supported by the National Science Foundation, Earth Sciences (EAR-1128799) and Department of Energy, Geosciences (DE-FG02-94ER14466). The Advanced Photon Source is supported by the U.S. Department of Energy, Office of Science, Basic Energy Sciences, under Contract No. W-31-109-Eng-38. We thank Joanne Stubbs and Peter Eng at GSECARS BM-13 for their assistance in data collection at the beamline. We thank Trevor Clark and Ke Wang from the Materials Characterization Lab at Penn State University for their help with transmission electron microscopy. Finally, we express our appreciation to two anonymous reviewers of this manuscript.

References

Ahmad, M.I. and Bhattacharya, S.S. (2009) Size effect on the lattice parameters of nanocrystalline anatase. Applied Physics Letters, 95, 191906 (3 pp).

Ardizzone, S. and Formaro, L. (1985) Hydrothermal preparation of goethite crystals. Surface Technology, 26, 269-274.

Avrami, M. (1939) Kinetics of phase change: I General Theory. Journal of Chemical Physics, 7, 1103-1112.

Avrami, M. (1940) Kinetics of phase change: II Transformation-time relations of random distribution of nuclei. Journal of Chemical Physics, 8, 212-224.

Ayyub, P., Multani, M., Barma, M., Palkar, V.R., and Vijayaraghavan, R. (1988) Size-induced structural phase transitions and hyperfine properties of microcrystalline Fe_2O_3. Journal of Physics C: Solid State Physics, 21, 2229-2245.

Ayyub, P., Palkar, V.R., Chattopadhyay, S., and Multani, M. (1995) Effect of crystal size reduction on lattice symmetry and cooperative properties. Physical Review B, 51, 6135-6138.

Baldinozzi, G., Simeone, D., Gosset, D., and Dutheil, M. (2003) Neutron diffraction study of the size-induced tetragonal to monoclinic phase transition in zirconia nanocrystals. Physical Review Letters, 90, 216103 (4 pp).

688 Bhowmik, R.N., Ranganathan, R., and Nagarajan, R. (2006) Lattice expansion and
689 noncollinear to collinear ferrimagnetic order in a $MnCr_2O_4$ nanoparticle.
690 Physical Review B, 73, 144413 (9 pp).

691 Blesa, M.A. and Matijević, E. (1989) Phase transformations of iron oxides,
692 oxohydroxides, and hydrous oxides in aqueous media. Advances in Colloid
693 and Interface Science, 29, 173-221.

694 Borchert, H., Shevchenko, E.V., Robert, A., Mekis, I., Kornowski, A., Grübel, G., and
695 Weller, H. (2005) Determination of nanocrystal sizes: A comparison of TEM,
696 SAXS, and XRD studies of highly monodisperse $CoPt_3$ particles. Langmuir, 21,
697 1931-1936.

698 Boswell, F.W.C. (1951) Precise determination of lattice constants by electron
699 diffraction and variations in the lattice constants of very small crystallites.
700 Proceedings of the Physical Society. Section A, 64, 465.

701 Burleson, D.J. and Penn, R.L. (2006) Two-step growth of goethite from ferrihydrite.
702 Langmuir, 22, 402-409.

703 Carlson, L., Bigham, J.M., Schwertmann, U., Kyek, A., and Wagner, F. (2002)
704 Scavenging of As from acid mine drainage by schwertmannite and
705 ferrihydrite: a comparison with synthetic analogues. Environmental Science
706 and Technology, 36, 1712-1719.

Chen, S.A., Heaney, P.J., Kubicki, J.D., and Post, J.E. (2018) A time-resolved synchrotron X-ray diffraction study of the transformation from ferrihydrite to goethite and hematite. Abstracts of the 2018 Goldschmidt Conference.

Chen, L., Fleming, P., Morris, V., Holmes, J.D., and Morris, M.A. (2010) Size-related lattice parameter changes and surface defects in ceria nanocrystals. The Journal of Physical Chemistry C, 114, 12909-12919.

Choi, C.J., Tolochko, O., and Kim, B.K. (2002) Preparation of iron nanoparticles by chemical vapor condensation. Materials Letters, 56, 289-294.

Cimino, A., Porta, P., and Valigi, M. (1966) Dependence of the lattice parameter of magnesium oxide on crystallite size. Journal of the American Ceramic Society, 49, 152-156.

Cocozza, C., Tsao, C.C., Cheah, S.F., Kraemer, S.M., Raymond, K.N., Miano, T.M., and Sposito, G. (2002) Temperature dependence of goethite dissolution promoted by trihydroxamate siderophores. Geochimica et Cosmochimica Acta, 66, 431-438.

Cornell, R.M. and Giovanoli, R. (1985) Effect of solution conditions on the proportion and morphology of goethite formed from ferrihydrite. Clays and Clay Minerals, 33, 424-432.

Cornell, R.M., Posner, A.M., and Quirk, J.P. (1976) Kinetics and mechanisms of the acid dissolution of goethite (α-FeOOH). Journal of Inorganic Nuclear Chemistry, 38, 563-567.

728 Cornell, R.M. and Schwertmann, U. (2003) The iron oxides: structure, properties,
729 reactions, occurrences, and uses. VCH Verlag, Weinheim.

730 Das S., Hendry, M., and Essilfie-Dughan, J. (2011) Transformation of two-line
731 ferrihydrite to goethite and hematite as a function of pH and temperature.
732 Environmental Science and Technology, 45, 268-275.

733 Davidson, L.E., Shaw, S., and Benning, L.G. (2008) The kinetics and mechanisms of
734 schwertmannite transformation to goethite and hematite under alkaline
735 conditions. American Mineralogist, 93, 1326-1337.

736 Davisson, C. and Germer, L.H. (1927) Diffraction of electrons by a crystal of nickel.
737 Physical Review, 30, 705.

738 Deshpande, S., Patil, S., Kuchibhatla, S.V.N.T., Seal, S. (2005) Size dependency
739 variation in lattice parameter and valency states in nanocrystalline cerium
740 oxide. Applied Physics Letters, 87, 133113 (3pp).

741 Diehm, P.M., Ágoston, P., and Albe, K. (2012) Size-Dependent Lattice Expansion in
742 Nanoparticles: Reality or Anomaly? ChemPhysChem, 13, 2443-2454.

743 Duan, Y. and Li, J. (2004) Structure study of nickel nanoparticles. Materials
744 Chemistry and Physics, 87, 452-454.

745 Fan, H., Song, B., and Li, Q. (2006) Thermal behavior of goethite during
746 transformation to hematite. Materials Chemistry and Physics, 98, 148-153.

747 Ferris, F.G., Tazaki, K., and Fyfe, W.S. (1989) Iron oxides in acid mine drainage
748 environments and their association with bacteria. Chemical Geology, 74, 321-
749 330.

750 Finch, G.I. and Fordham, S. (1936) The effect of crystal-size on lattice-dimensions.
751 Proceedings of the Physical Society, 48, 85.

752 Finch, G.I. and Wilman, H. (1934) 163. The lattice dimensions of zinc oxide. Journal
753 of the Chemical Society, 751-754. [Note to Editor: No volume number for this
754 article]

755 Fukuhara, M. (2003) Lattice expansion of nanoscale compound particles. Physics
756 Letters A, 313, 427-430.

757 Gilbert, B., Lu, G., and Kim, C.S. (2007) Stable cluster formation in aqueous
758 suspensions of iron oxyhydroxide nanoparticles. Journal of Colloid and
759 Interface Science, 313, 152-159.

760 Goldstein, A.N., Echer, C.M., and Alivisatos, A.P. (1992) Melting in semiconductor
761 nanocrystals. Science, 256, 1425-1427.

762 Goss, C.J. (1987) The kinetics and reaction mechanism of the goethite to hematite
763 transformation. Mineralogical Magazine, 51, 437-451.

764 Gualtieri, A.F. and Venturelli, P. (1999) In situ study of the goethite-hematite phase
765 transformation by real time synchrotron powder diffraction. American
766 Mineralogist, 84, 895-904.

767 Guyodo, Y., Mostrom, A., Lee Penn, R., and Banerjee, S.K. (2003) From nanodots to
768 nanorods: Oriented aggregation and magnetic evolution of nanocrystalline
769 goethite. Geophysical Research Letters, 30, doi.org/10.1029/2003GL017021.

770 Hailstone, R. K., DiFrancesco, A. G., Leong, J. G., Allston, T. D., and Reed, K. J. (2009) A
771 study of lattice expansion in CeO_2 nanoparticles by transmission electron
772 microscopy. The Journal of Physical Chemistry C, 113, 15155-15159.

773 Heaney, P.J. (2000) Phase transformations induced by solid solution. Reviews in
774 Mineralogy and Geochemistry, 39, 135-174.

775 Hochella, M.F., Lower, S.K., Maurice, P.A., Penn, R.L., Sahai, N., Sparks, D.L., and
776 Twining, B.S. (2008) Nanominerals, mineral nanoparticles, and earth systems.
777 Science, 319, 1631-1635.

778 Holzwarth, U. and Gibson, N. (2011) The Scherrer equation versus the'Debye-
779 Scherrer equation'. Nature Nanotechnology, 6, 534.

780 Hoshina, T., Kakemoto, H., Tsurumi, T., Wada, S., and Yashima, M. (2006) Size and
781 temperature induced phase transition behaviors of barium titanate
782 nanoparticles. Journal of Applied Physics, 99, 054311 (8 pp).

783 Hummer, D.R., Heaney, P.J., and Post, J.E. (2012) In situ observations of particle size
784 evolution during the hydrothermal crystallization of TiO_2: A time-resolved
785 synchrotron SAXS and WAXS study. Journal of Crystal Growth, 344, 51-58.

786 Hyland, E.G., Sheldon, N.D., Van der Voo, R., Badgley, C., and Abrajevitch, A. (2015) A
787 new paleoprecipitation proxy based on soil magnetic properties:

Implications for expanding paleoclimate reconstructions. Geological Society of America Bulletin. 127, 975-981.

Johnson, W.A. and Mehl, R.F. (1939) Reaction kinetics in processes of nucleation and growth. Transactions of the American Institute of Mining, Metallurgical and Petroleum Engineers, 135, 416-458.

Johnston, J.H. and Lewis, D.G. (1983) A detailed study of the transformation of ferrihydrite to hematite in an aqueous medium at 92 C. Geochimica et Cosmochimica Acta, 47, 1823-1831.

Kämpf, N. and Schwertmann, U. (1983) Goethite and hematite in a climosequence in southern Brazil and their application in classification of kaolinitic soils. Geoderma, 29, 27-39.

Koga, K., Ikeshoji, T., and Sugawara, K. I. (2004) Size-and temperature-dependent structural transitions in gold nanoparticles. Physical Review Letters, 92, 115507.

Kossoy, A., Feldman, Y., Wachtel, E., Gartsman, K., Lubomirsky, I., Fleig, J., and Maier, J. (2006) On the origin of the lattice constant anomaly in nanocrystalline ceria. Physical Chemistry Chemical Physics, 8, 1111-1115.

Kuznetsov, A.Y., Machado, R., Gomes, L.S., Achete, C.A., Swamy, V., Muddle, B.C., and Prakapenka, V. (2009) Size dependence of rutile TiO 2 lattice parameters determined via simultaneous size, strain, and shape modeling. Applied Physics Letters, 94, 193117.

809 Kwei, G. H., Lawson, A. C., Billinge, S.J.L., and Cheong, S.W. (1993) Structures of the
810 ferroelectric phases of barium titanate. The Journal of Physical Chemistry, 97,
811 2368-2377.

812 Larson, A.C., and Von Dreele, R.B. (2004) General Structure Analysis System (GSAS).
813 Los Alamos National Laboratory Report LAUR 86-748.

814 Lennard-Jones, J.E. (1930) Note on the Dependence of Crystal Spacing on Crystal
815 Size. Zeitschrift für Kristallographie-Crystalline Materials, 75, 215-216.

816 Lennard-Jones, J.E. and Dent, B.M. (1928) The change in lattice spacing at a crystal
817 boundary. Transactions of the Faraday Society, 24, 92-108.

818 Mays, C.W., Vermaak, J.S., and Kuhlmann-Wilsdorf, D. (1968) On surface stress and
819 surface tension: II. Determination of the surface stress of gold. Surface
820 Science, 12, 134-140.

821 Michel, F.M., Barrón, V., Torrent, J., Morales, M.P., Serna, C.J., Boily, J.F., Liu, Q.,
822 Ambrosini, A., Cismasu, A.C., and Brown, G.E. (2010) Ordered ferrimagnetic
823 form of ferrihydrite reveals links among structure, composition, and
824 magnetism. Proceedings of the National Academy of Sciences, 107, 2787-
825 2792.

826 Murray, J., Kirwan, L., Loan, M., and Hodnett, B.K. (2009) In-situ synchrotron
827 diffraction study of the hydrothermal transformation of goethite to hematite
828 in sodium aluminate solutions. Hydrometallurgy, 95, 239-246.

Navrotsky, A. (2009) Energetics of oxide nanoparticles. Internationl Journal of Quantum Chemistry, 109, 2647-2657.

Norby, P. (1996) In-situ time resolved synchrotron powder diffraction studies of syntheses and chemical reactions. Materials Science Forum, 228-231, 147-152.

Panomsuwan, G. and Manuspiya, H. (2019) Correlation between size and phase structure of crystalline $BaTiO_3$ particles synthesized by sol-gel method. Materials Research Express, 6, 065062.

Parise, J.B., Cahill, C.L., and Lee, Y. (2000) Dynamic powder crystallography with synchrotron X-ray sources. Canadian Mineralogist, 38, 777-800.

Pawlow, P. (1909). Über die Abhängigkeit des Schmelzpunktes von der Oberflächenenergie eines festen Körpers. Zeitschrift für physikalische Chemie, 65, 1-35.

Penn, R.L., Erbs, J.J., and Gulliver, D.M. (2006) Controlled growth of alpha-FeOOH nanorods by exploiting-oriented aggregation. Journal of Crystal Growth, 293, 1-4.

Perebeinos, V., Chan, S.W., and Zhang, F. (2002) 'Madelung model' prediction for dependence of lattice parameter on nanocrystal size. Solid State Communications, 123, 295-297.

Peterson, K.M., Heaney, P.J., Post, J.E., and Eng, P.J. (2015) A refined monoclinic structure for a variety of "hydrohematite". American Mineralogist, 100, 570-579.

Peterson, K.M., Heaney, P.J., and Post, J.E. (2016) A kinetic analysis of the transformation from akaganeite to hematite: An in situ time-resolved X-ray diffraction study. Chemical Geology, 444, 27-36.

Peterson, K.M., Heaney, P.J., and Post, J.E. (2018) Evolution in the structure of akaganeite and hematite during hydrothermal growth: An in situ synchrotron X-ray diffraction analysis. Powder Difffraction, 33, 287-297.

Pickup, E. (1936) Anomalous values of lattice spacings obtained by electron diffraction. Nature, 137, 1072.

Prescher, C. and Prakapenka, V.B. (2015) *DIOPTAS*: A program for reduction of two-dimensional X-ray diffraction data and data exploration. High Pressure Research, 35, 223-230.

Qadri, S.B., Skelton, E.F., Hsu, D., Dinsmore, A.D., Yang, J., Gray, H.F., and Ratna, B.R. (1999) Size-induced transition-temperature reduction in nanoparticles of ZnS. Physical Review B, 60, 9191-9193.

Randall, J.T. and Rooksby, H.P. (1932) Polish on metals. Nature, 129, 280-281.

Rellinghaus, B., Stappert, S., Wassermann, E.F., Sauer, H. and Spliethoff, B. (2001) The effect of oxidation on the structure of nickel nanoparticles. The European

Physical Journal D-Atomic, Molecular, Optical and Plasma Physics. 16, 249-252.

Rivest, J.B., Fong, L.K., Jain, P.K., Toney, M. F., and Alivisatos, A.P. (2011) Size dependence of a temperature-induced solid–solid phase transition in copper (I) sulfide. The Journal of Physical Chemistry Letters, 2, 2402-2406.

Rodenbough, P.P., Zheng, C., Liu, Y., Hui, C., Xia, Y., Ran, Z., Hu, Y. and Chan, S.W. (2017) Lattice expansion in metal oxide nanoparticles: MgO, Co_3O_4, and Fe_3O_4. Journal of the American Ceramic Society, 100, 384-392.

Scherrer, P. (1918) Bestimmung der Grösse und der inneren Struktur von Kolloidteilchen mittels Röntgenstrahlen. Nachrichten von der Gesellschaft der Wissenschaften zu Göttingen, Mathematisch-Physikalische Klasse, 98-100

Schlag, S., and Eicke, H.F. (1994) Size driven phase transition in nanocrystalline $BaTiO_3$. Solid state communications, 91, 883-887.

Schwertmann, U., Cambier, P., and Murad, E. (1985) Properties of goethites of varying crystallinity. Clays and Clay Minerals, 33, 369-378.

Schwertmann, U. and Cornell, R.M. (2000) Iron oxides in the laboratory. Wiley-VCH, Weinheim.

Schwertmann, U., Stanjek, H., and Becher, H.H. (2004) Long-term in vitro transformation of 2-line ferrihydrite to goethite/hematite at 4, 10, 15 and 25ºC. Clay Minerals, 39, 433-438.

889 Sharma, M., Murugavel, S., Shukla, D.K., and De Groot, F.M. (2018) Reversal in the
890 lattice contraction of α-Fe_2O_3 nanoparticles. The Journal of Physical
891 Chemistry C, 122, 9292-9301.

892 Sharma, V.K., Filip, J., Zboril, R., and Varma, R.S. (2015) Natural inorganic
893 nanoparticles–formation, fate, and toxicity in the environment. Chemical
894 Society Reviews, 44, 8410-8423.

895 Shaw, S., Pepper, S.E., Bryan, N.D., and Livens, F.R. (2005) The kinetics and
896 mechanisms of goethite and hematite crystallization under alkaline
897 conditions, and in the presence of phosphate. American Mineralogist, 90,
898 1852-1860.

899 Shi, C., Billinge, S.J., Puma, E., Bang, S.H., Bean, N.J., de Sugny, J.C., Gambee, R.G.,
900 Haskell, R.C., Hightower, A., and Monson, T.C. (2018) Barium titanate
901 nanoparticles: Short-range lattice distortions with long-range cubic order.
902 Physical Review B, 98, 085421.

903 Sidhu, P.S., Gilkes, R.J., Cornell, R.M., and Posner, A.M. (1981) Dissolution of iron
904 oxides and oxyhydroxides in hydrochloric and perchloric acids. Clays and
905 Clay Minerals, 29, 269-276.

906 Smith, M.B., Page, K., Siegrist, T., Redmond, P.L., Walter, E.C., Seshadri, R., Brus, L.E.,
907 and Steigerwald, M.L. (2008) Crystal structure and the paraelectric-to-
908 ferroelectric phase transition of nanoscale $BaTiO_3$. Journal of the American
909 Chemical Society, 130, 6955-6963.

910 Solliard, C., and Flueli, M. (1985) Surface stress and size effect on the lattice
911 parameter in small particles of gold and platinum. Surface Science, 156, 487-
912 494.

913 Soltis, J.A., Feinberg, J.M., Gilbert, B., and Penn, R.L. (2016) Phase transformation and
914 particle-mediated growth in the formation of hematite from 2-line
915 ferrihydrite. Crystal Growth and Design, 16, 922-932.

916 Song, J., Rodenbough, P.P., Zhang, L., and Chan, S.W. (2016) Size-Dependent Crystal
917 Properties of Nanocuprite. International Journal of Applied Ceramic
918 Technology, 13, 389-394.

919 Spanier, J.E., Robinson, R.D., Zhang, F., Chan, S.W., and Herman, I.P. (2001) Size-
920 dependent properties of CeO_{2-y} nanoparticles as studied by Raman scattering.
921 Physical Review B, 64, 245407.

922 Stemig, A.M., Do, T.A., Yuwono, V.M., Arnold, W.A., and Penn, R.L. (2014) Goethite
923 nanoparticle aggregation: Effects of buffers, metal ions, and 4-
924 chloronitrobenzene reduction. Environmental Science: Nano, 1, 478-487.

925 Sun, C., Li, H., and Chen, L. (2012) Nanostructured ceria-based materials: synthesis,
926 properties, and applications. Energy & Environmental Science, 5, 8475-8505.

927 Sun, J. and Simon, S.L. (2007) The melting behavior of aluminum nanoparticles.
928 Thermochimica Acta, 463, 32-40.

929 Szytuła, A., Burewicz, A., Dimitrijević, Ž., Kraśnicki, S., Rżany, H., Todorović, J., Wanic,
930 A., Wolski, W. (1968) Neutron diffraction studies of α-FeOOH. Physica Status
931 Solidi, 26, 429-434.

932 Takagi M. (1954) Electron-Diffraction Study of Liquid-Solid Transition of Thin Metal
933 Films. Journal of the Physical Society of Japan. 9, 359-363.

934 Thompson, P., Cox, D.E., and Hastings, J.B. (1987) Rietveld refinement of Debye-
935 Scherrer synchrotron X-ray data from Al_2O_3. Journal of Applied
936 Crystallography, 20, 79-83.

937 Toby, B.H. (2001) EXPGUI, a graphical user interface for GSAS. Journal of Applied
938 Crystallography, 34, 210-213.

939 Tolbert, S.H., and Alivisatos, A.P. (1994) Size dependence of a first order solid-solid
940 phase transition: The wurtzite to rock salt transformation in CdSe
941 nanocrystals. Science, 265, 373-376.

942 Trovarelli, A. and Llorca, J. (2017) Ceria catalysts at nanoscale: how do crystal
943 shapes shape catalysis? ACS Catalysis, 7, 4716-4735.

944 Tsunekawa, S., Ito, S., Mori, T., Ishikawa, K., Li, Z. Q., and Kawazoe, Y. (2000) Critical
945 size and anomalous lattice expansion in nanocrystalline $BaTiO_3$ particles.
946 Physical Review B, 62, 3065.

947 Tsunekawa, S., Sahara, R., Kawazoe, Y., and Ishikawa, K. (1999) Lattice relaxation of
948 monosize CeO_{2-x} nanocrystalline particles. Applied Surface Science, 152, 53-
949 56.

Walter, D., Buxbaum, G., and Laqua, W. (2001) The mechanism of the thermal transformation from goethite to hematite. Journal of Thermal Analysis and Calorimetry, 63, 733-748.

Wasserman, H.J. and Vermaak, J.S. (1970) On the determination of a lattice contraction in very small silver particles. Surface Science, 22, 164-172.

Wasserman, H.J. and Vermaak, J.S. (1972) On the determination of the surface stress of copper and platinum. Surface Science, 32, 168-174.

Waychunas, G.A., Kim, C.S., and Banfield, J.F. (2005) Nanoparticulate iron oxide minerals in soils and sediments: unique properties and contaminant scavenging mechanisms. Journal of Nanoparticle Research, 7, 409-433.

Wu, L., Wiesmann, H.J., Moodenbaugh, A.R., Klie, R.F., Zhu, Y., Welch, D.O., and Suenaga, M. (2004) Oxidation state and lattice expansion of CeO_{2-x} nanoparticles as a function of particle size. Physical Review B, 69, 125415.

Yee, N., Shaw, S., Benning, L.G., and Nguyen, T.H. (2006) The rate of ferrihydrite transformation to goethite via the Fe (II) pathway. American Mineralogist, 91, 92-96.

Zhang, F., Chan, S.W., Spanier, J.E., Apak, E., Jin, Q., Robinson, R.D., and Herman, I.P. (2002) Cerium oxide nanoparticles: size-selective formation and structure analysis. Applied Physics Letters, 80, 127-129.

970 **Figure Captions**

971

972 **Fig. 1** Environmental cell used for hydrothermal experiments. A) MAR165 CCD
973 detector; B) Forced-air heater; C) Polyimide capillary

974

975 **Fig. 2** (A) Low-magnification bright-field TEM image of synthetic goethite fibers
976 synthesized at 90 °C at pH 13 for 4 hr. (B) Higher magnification TEM image
977 revealing nanoscale crystallites within the fibers.

978

979 **Fig. 3.** Stacked TRXRD patterns showing the crystallization of goethite from 2-line
980 ferrihydrite at pH 13.6 at 90 °C.

981 **Fig. 4** X-ray diffraction patterns analyzed by means of Rietveld analysis at 90 °C
982 after 7 hr. Black crosses represent the observed pattern. The red line is the
983 calculated pattern. The blue line is the difference between the observed and
984 calculated patterns. The green line is the refined background.

985 **Fig. 5** The evolution of goethite crystallite size as ferrihydrite was heated at 90 °C
986 as a function of heating time.

987 **Fig. 6** The lattice parameters all decreased as crystallite size increased during the
988 transformation of ferrihydrite to goethite at 90 °C (blue diamonds, upper
989 horizontal axes). Thermal response data of natural goethite (from Gualtieri
990 and Venturelli 1999) are included for comparison (red squares, lower
991 horizontal axes). Synthetic goethite lattice parameters at room

temperature based on neutron diffraction (Szytuła et al. 1968) also are plotted (green triangles).

Fig. 7 Reaction rates for the crystallization of goethite from 2-line ferrihydrite as determined by the JMAK equation. Alpha (Eq. 3) , a measure of reaction progress, was calculated as the specified scale factor as a fraction of the maximum scale factor.

Fig. 8 Arrhenius plot of data from the crystallization of goethite from 2-line ferrihydrite.

Fig. 9 The variations of Fe-O2 bond length and Fe-O2-Fe and O2-Fe-O2 bond angles with particle size (blue diamonds, upper horizontal axes) during heating at 90 ^{o}C. For comparison, thermal expansion data of Gualtieri and Venturelli (1999) are plotted as reverse temperature (red squares, lower horizontal axes).

Supplementary Information—Figure 1. Variations of lattice parameters as a function of crystallite size. Au: Solliard and Flueli (1985); Pt: Wasserman and Vermaak (1970b); Ag: Wasserman and Vermaak (1970a); Cu_2O: Song et al. (2016); Fe_2O_3: Sharma et al. (2018); Fe_3O_4: Rodenbough et al. (2016); Co_3O_4: Rodenbough et al. (2016); MgO: Rodenbough et al. (2016); CeO_2: Zhang et al. (2002); FeOOH: This study; $MnCr_2O_4$: Bhowmik et al. (2006)

This is a preprint, the final version is subject to change, of the American Mineralogist (MSA)
Cite as Authors (Year) Title. American Mineralogist, in press.
DOI: https://doi.org/10.2138/am-2020-7217

Tables

Table 1. Kinetic analysis of the crystallization of goethite

Temp (^{o}C)	k (s^{-1})
80	$1.00(1) \times 10^{-4}$
90	$2.1(1) \times 10^{-4}$
100	$3.9(1) \times 10^{-4}$
E_a (kJ/mol)	73.6 ± 0.2

This is a preprint, the final version is subject to change, of the American Mineralogist (MSA)
Cite as Authors (Year) Title. American Mineralogist, in press.
DOI: https://doi.org/10.2138/am-2020-7217

Table 2. Linear coefficients of nanoscale contraction (CNCs) for selected materials.

Material	Crystallite Size Range (nm)	Linear CNC (nm^{-1}) x 10^4	CNC axis	Ref.
Au	3 to 12	7.37	a	Solliard and Flueli (1985)
Pt	3 to 25	2.76	a	Wasserman and Vermaak (1970b)
Ag	4 to 18	2.44	a	Wasserman and Vermaak (1970a)
α-Fe_2O_3	15 to 30	1.87	a	Sharma et al. (2018)
α -Fe_2O_3	15 to 30	1.36	c	Sharma et al. (2018)
α -Fe_2O_3	30 to 75	-0.12	a	Sharma et al. (2018)
α -Fe_2O_3	30 to 75	-0.13	c	Sharma et al. (2018)
Cu_2O	9 to 72	-0.32	a	Song et al. (2016)
Fe_3O_4	11 to 21	-0.76	a	Rodenbough et al. 2016
Co_3O_4	9 to 30	-0.96	a	Rodenbough et al. 2016
MgO	8 to 31	-1.51	a	Rodenbough et al. 2016
CeO_2	6 to 25	-2.42	a	Zhang et al. (2002)
α-FeOOH	9 to 19	-5.34	c	This study
$MnCr_2O_4$	11 to 19	-9.21	a	Bhowmik et al. (2006)

This is a preprint, the final version is subject to change, of the American Mineralogist (MSA)
Cite as Authors (Year) Title. American Mineralogist, in press.
DOI: https://doi.org/10.2138/am-2020-7217

Ms. 7217 – Revision 1

Figures

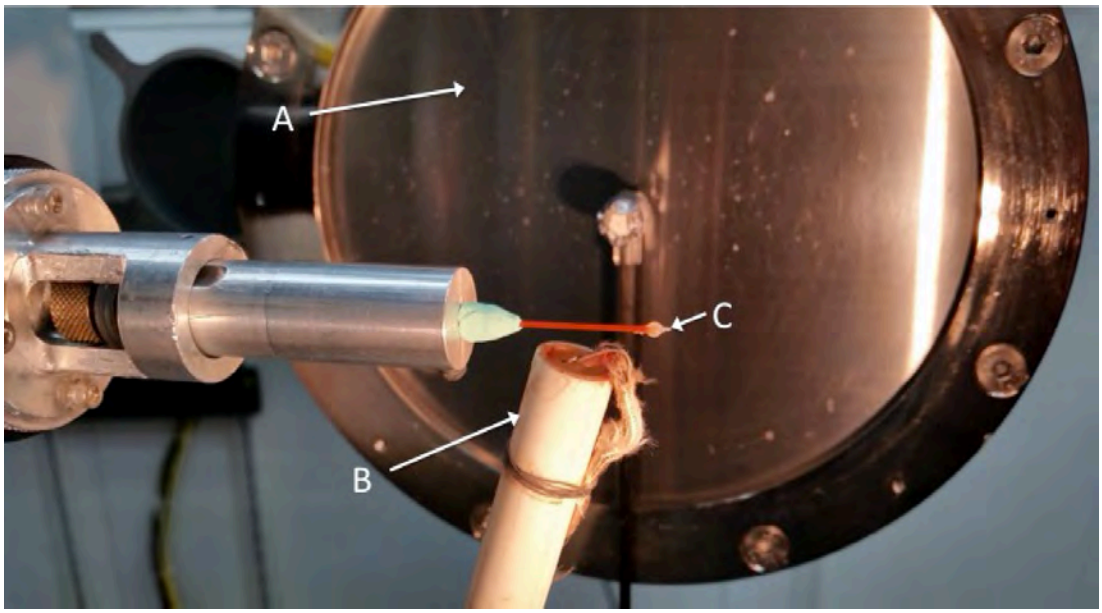

Figure 1. Environmental cell used for hydrothermal experiments. A) MAR165 CCD detector; B) Forced-air heater; C) Polyimide capillary

This is a preprint, the final version is subject to change, of the American Mineralogist (MSA)
Cite as Authors (Year) Title. American Mineralogist, in press.
DOI: https://doi.org/10.2138/am-2020-7217

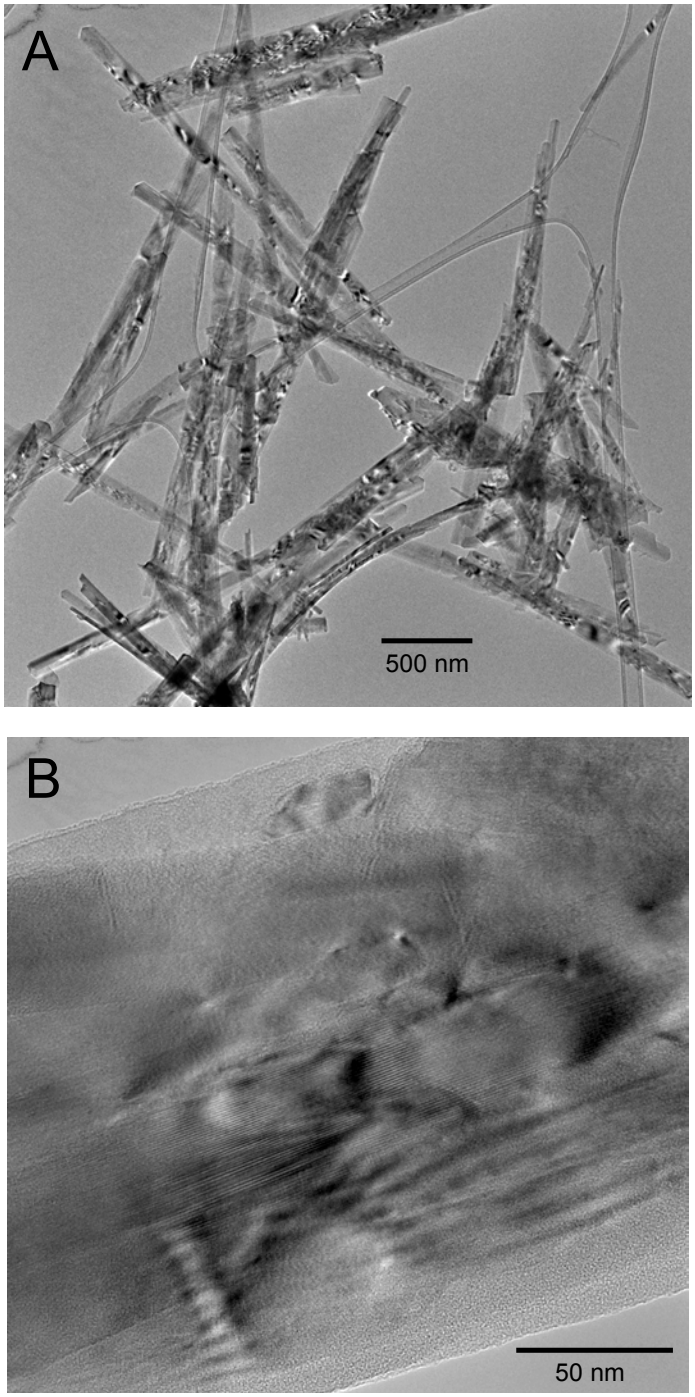

Figure 2. (A) Low-magnification bright-field TEM image of goethite fibers synthesized at 90 °C at pH 13 for 4 hr. (B) Higher magnification TEM image revealing nanoscale crystallite domains within the fibers.

This is a preprint, the final version is subject to change, of the American Mineralogist (MSA)
Cite as Authors (Year) Title. American Mineralogist, in press.
DOI: https://doi.org/10.2138/am-2020-7217

Ms. 7217 – Revision 1

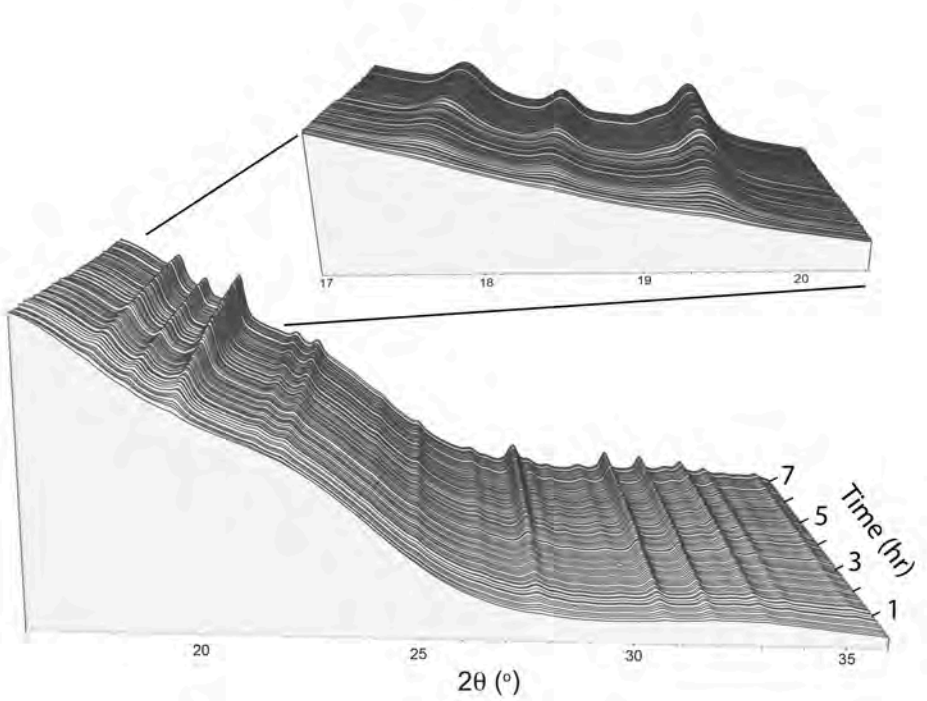

Figure 3. Stacked TRXRD pattern showing the crystallization of goethite from 2-line ferrihydrite at pH 13.6 at 90 °C.

This is a preprint, the final version is subject to change, of the American Mineralogist (MSA)
Cite as Authors (Year) Title. American Mineralogist, in press.
DOI: https://doi.org/10.2138/am-2020-7217

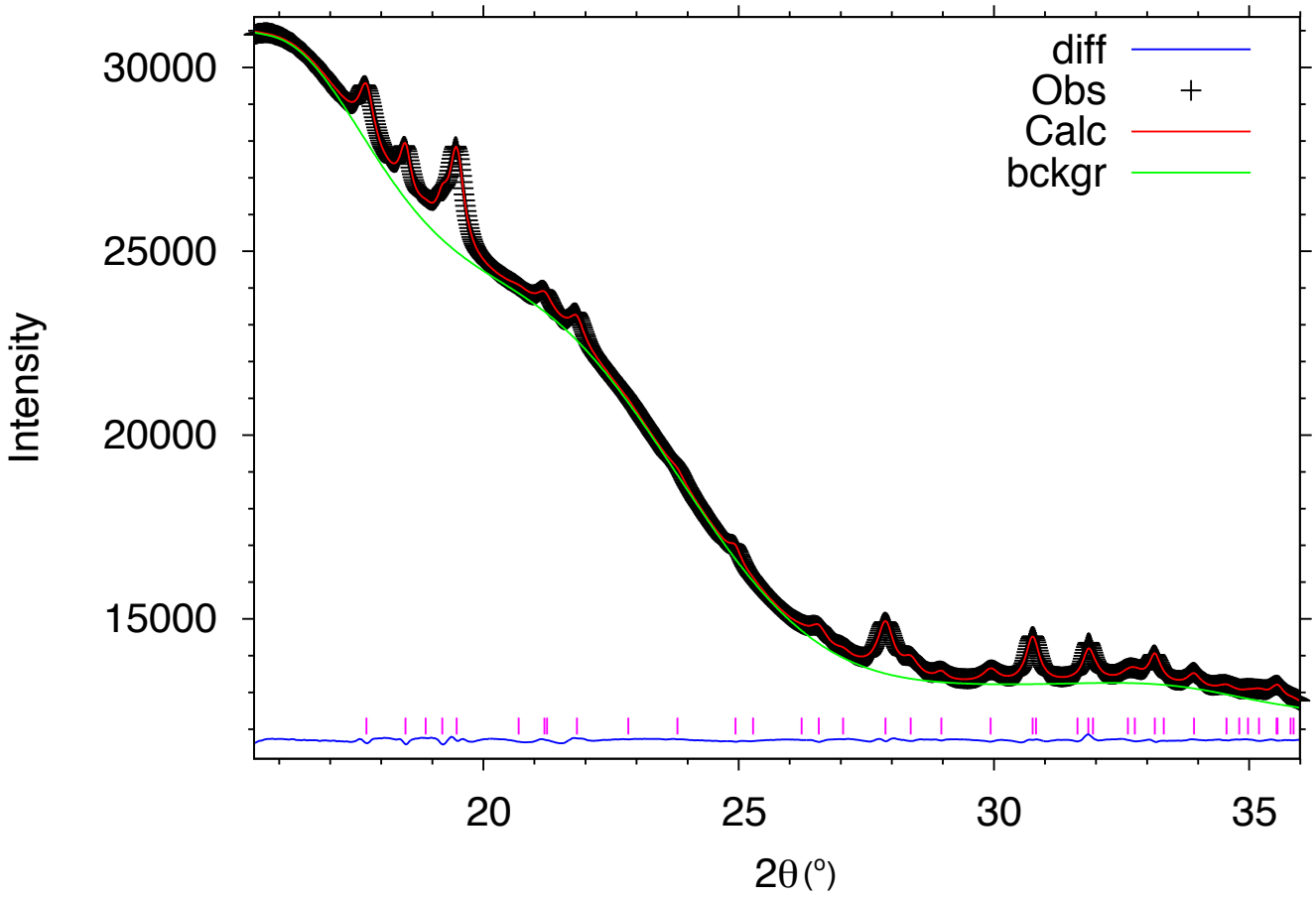

Figure 4. X-ray diffraction patterns analyzed by means of Rietveld analysis at 90 °C after 7 hr. Black crosses represent the observed pattern. The red line is the calculated pattern. The blue line is the difference between the observed and calculated patterns. The green line is the refined background.

This is a preprint, the final version is subject to change, of the American Mineralogist (MSA)
Cite as Authors (Year) Title. American Mineralogist, in press.
DOI: https://doi.org/10.2138/am-2020-7217

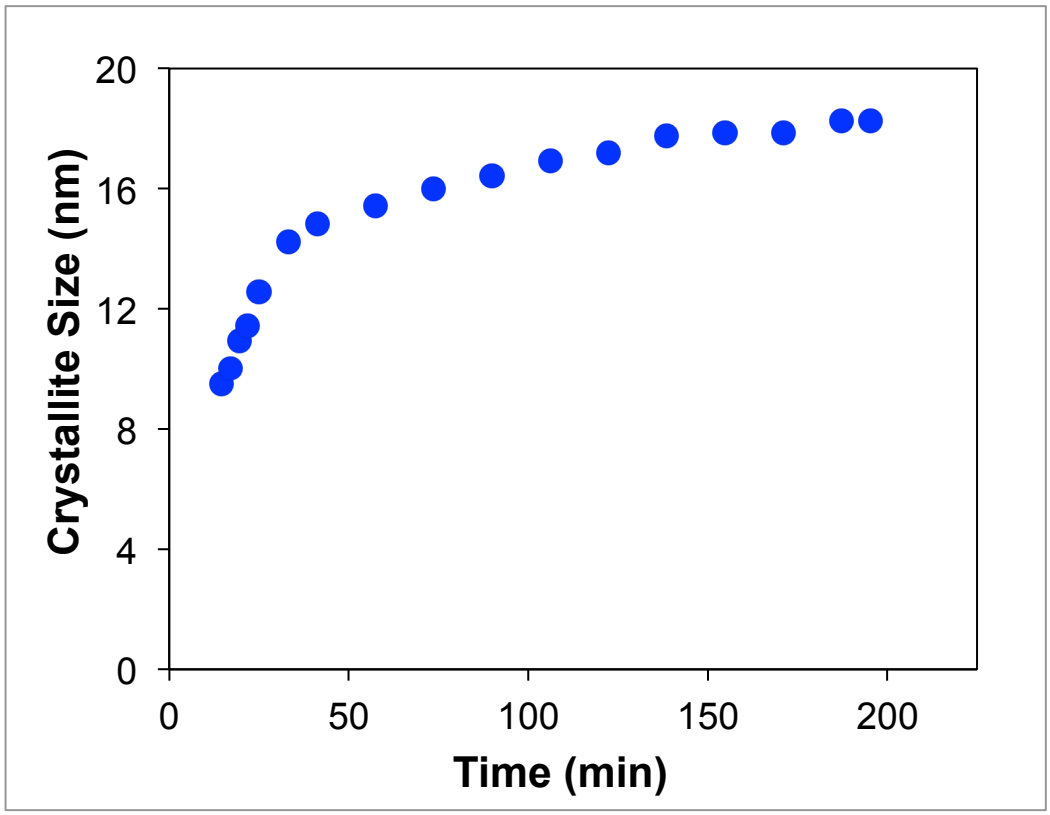

Figure 5. The evolution of goethite crystallite size as ferrihydrite was heated at 90 ^{o}C as a function of heating time.

This is a preprint, the final version is subject to change, of the American Mineralogist (MSA)
Cite as Authors (Year) Title. American Mineralogist, in press.
DOI: https://doi.org/10.2138/am-2020-7217

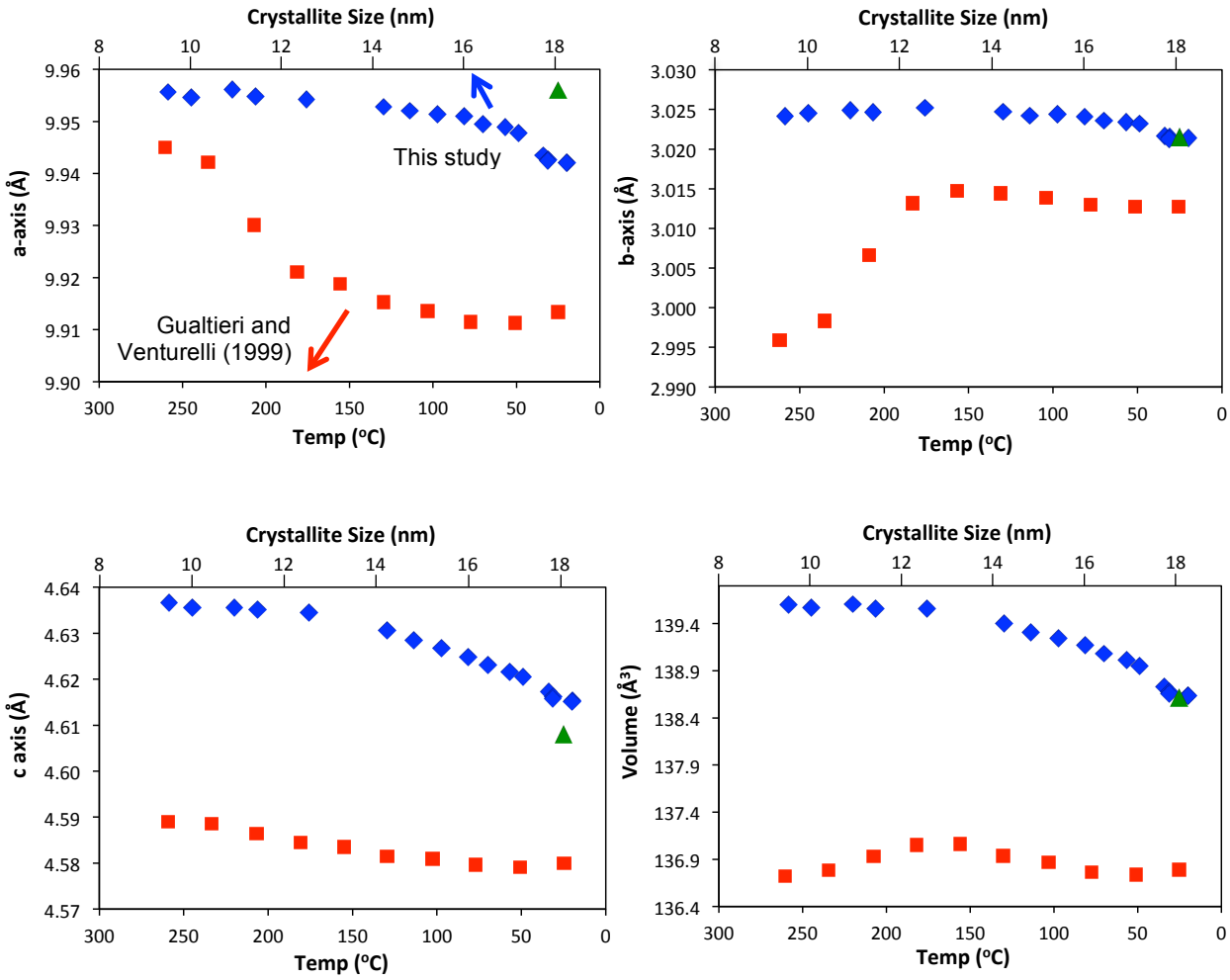

Figure 6. The lattice parameters all decreased as crystallite size increased during the transformation of ferrihydrite to goethite at 90 °C (blue diamonds, upper horizontal axes). Thermal response data of synthetic goethite (from Gualtieri and Venturelli 1999) are included for comparison (red squares, lower horizontal axes). Synthetic goethite lattice parameters at room temperature based on neutron diffraction (Szytuła et al. 1968) also are plotted (green triangles).

This is a preprint, the final version is subject to change, of the American Mineralogist (MSA)
Cite as Authors (Year) Title. American Mineralogist, in press.
DOI: https://doi.org/10.2138/am-2020-7217

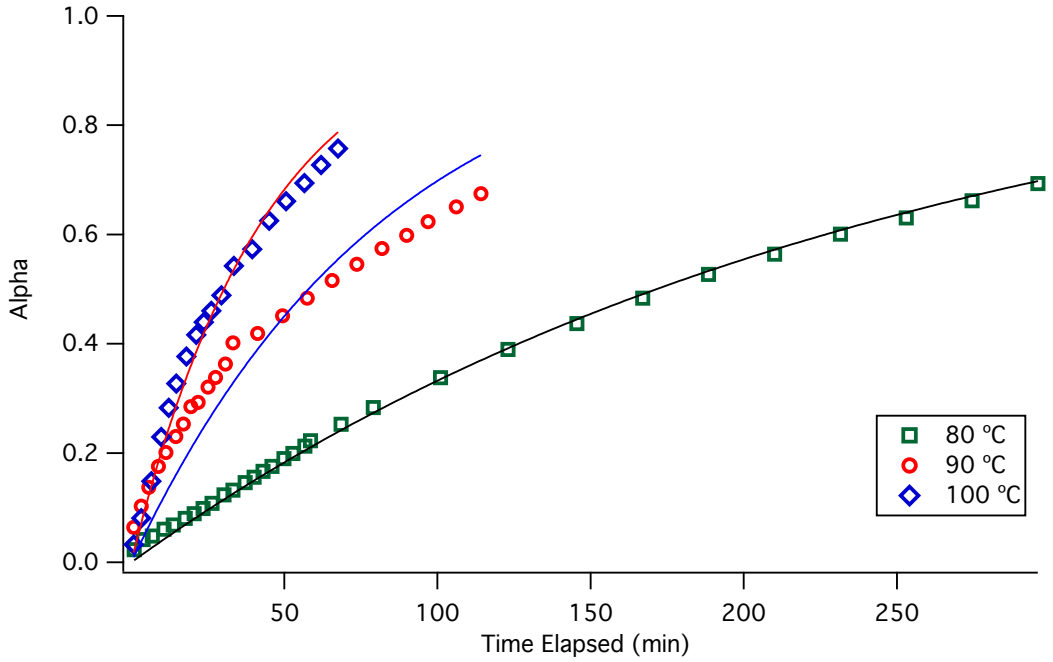

Figure 7. Reaction rates for the crystallization of goethite from 2-line ferrihydrite as determined by the JMAK equation. Alpha (Eq. 3), a measure of reaction progress, was calculated as the specified scale factor as a fraction of the maximum scale factor.

This is a preprint, the final version is subject to change, of the American Mineralogist (MSA)
Cite as Authors (Year) Title. American Mineralogist, in press.
DOI: https://doi.org/10.2138/am-2020-7217

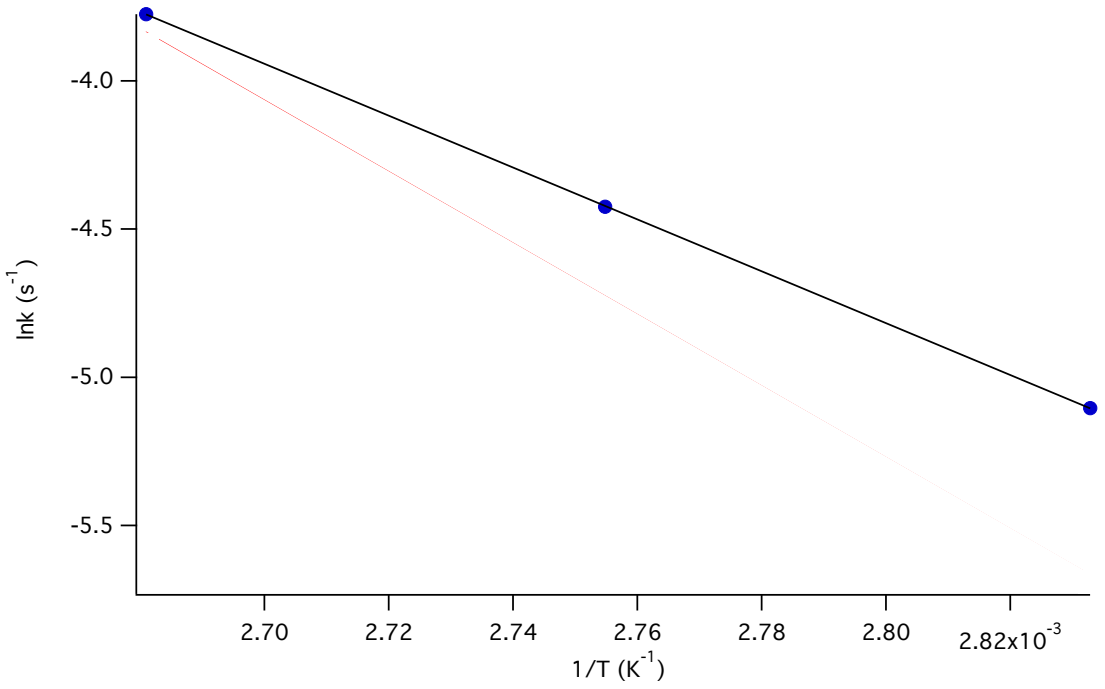

Figure 8. Arrhenius plot of data from the crystallization of goethite from 2-line ferrihydrite.

This is a preprint, the final version is subject to change, of the American Mineralogist (MSA)
Cite as Authors (Year) Title. American Mineralogist, in press.
DOI: https://doi.org/10.2138/am-2020-7217

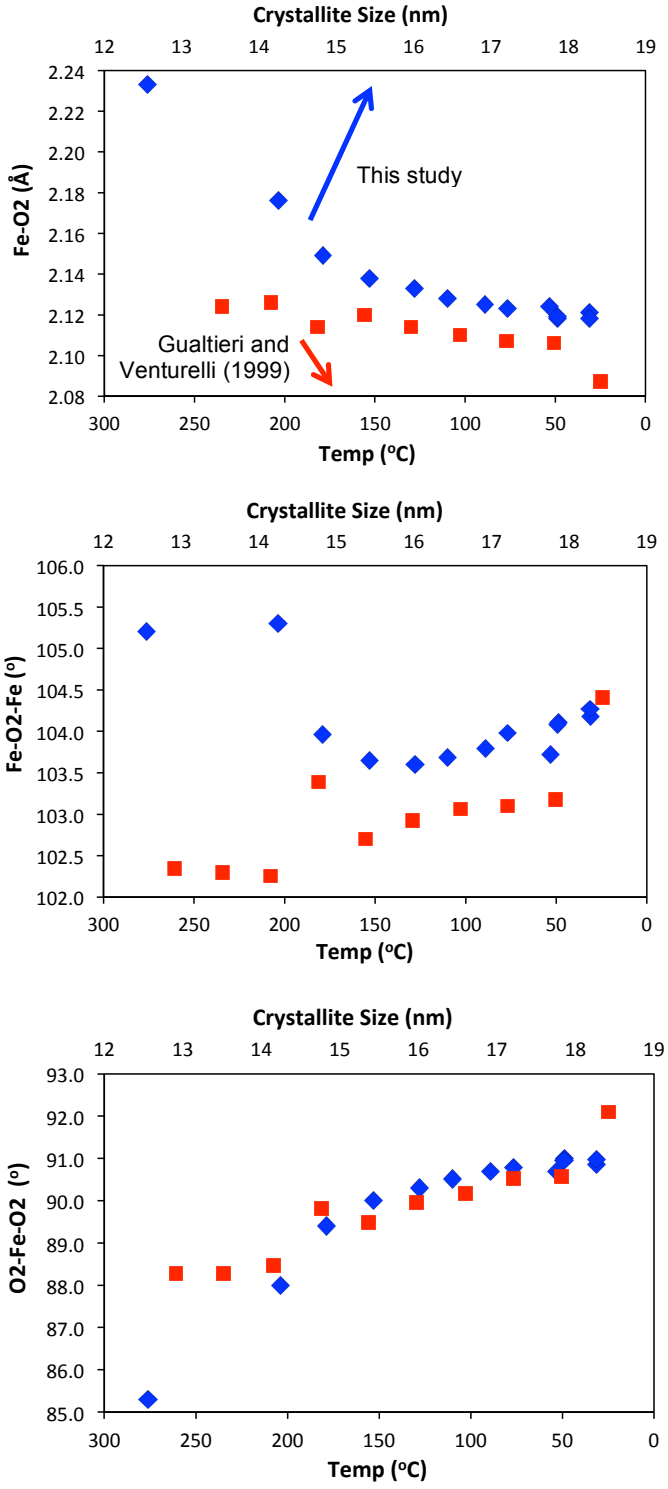

Figure 9. The variations of Fe-O2 bond length and Fe-O2-Fe and O2-Fe-O2 bond angles with particle size (blue diamonds, upper horizontal axes) during heating at 90 °C. For comparison, thermal expansion data of Gualtieri and Venturelli (1999) are plotted as reverse temperature (red squares, lower horizontal axes).

This is a preprint, the final version is subject to change, of the American Mineralogist (MSA)
Cite as Authors (Year) Title. American Mineralogist, in press.
DOI: https://doi.org/10.2138/am-2020-7217

Ms. 7217 – Revision 1

Supplementary Information

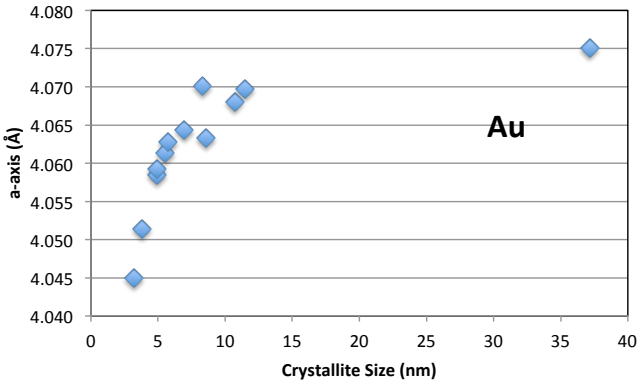

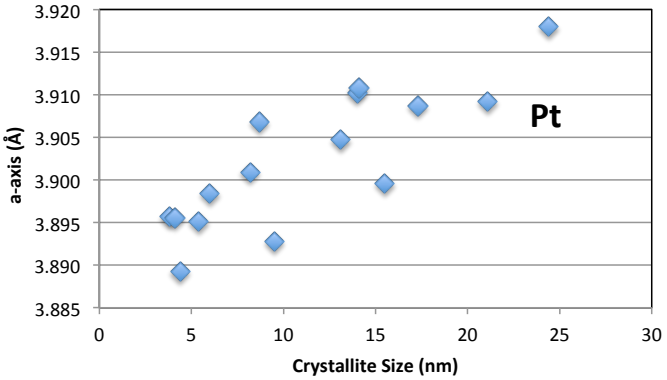

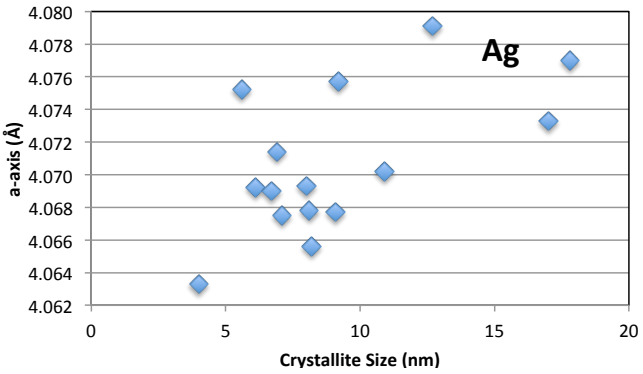

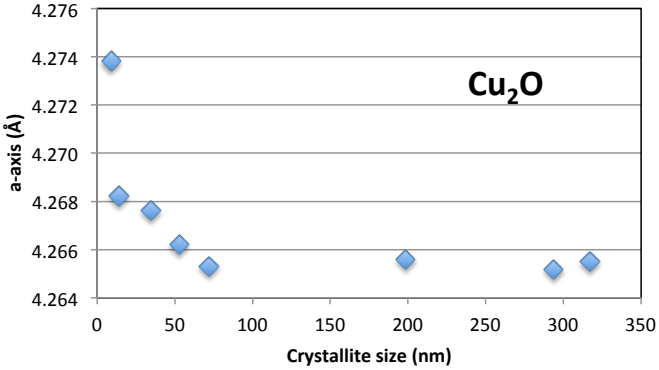

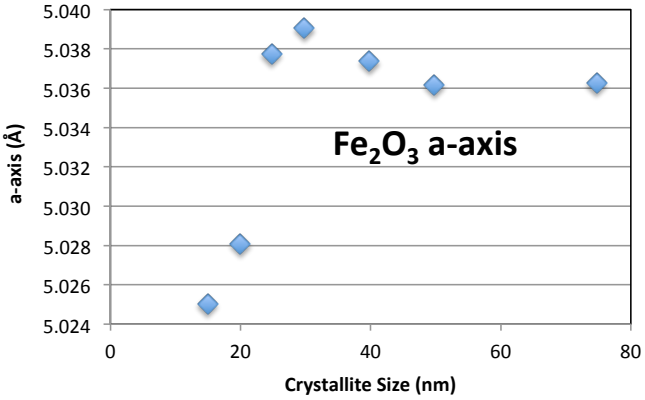

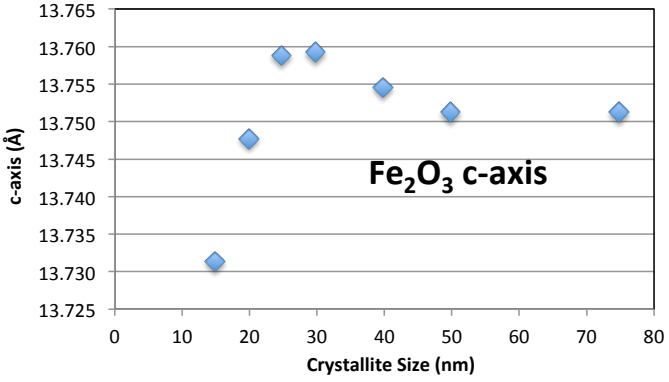

This is a preprint, the final version is subject to change, of the American Mineralogist (MSA)
Cite as Authors (Year) Title. American Mineralogist, in press.
DOI: https://doi.org/10.2138/am-2020-7217

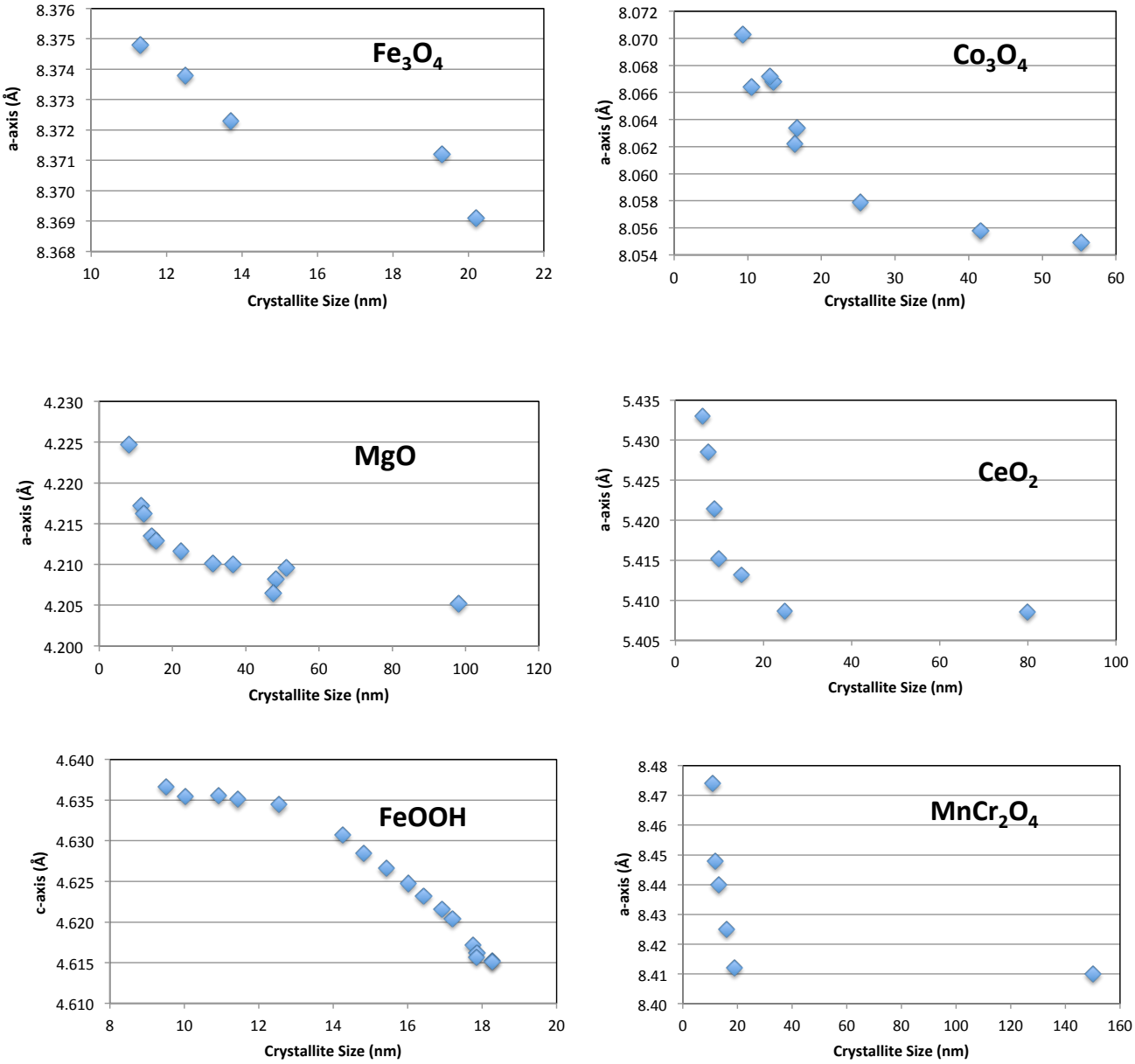

Supplementary Information—Figure 1. Variations of lattice parameters as a function of crystallite size. Au: Solliard and Flueli (1985); Pt: Wasserman and Vermaak (1970b); Ag: Wasserman and Vermaak (1970a); Cu_2O: Song et al. (2016); Fe_2O_3: Sharma et al. (2018); Fe_3O_4: Rodenbough et al. (2016); Co_3O_4: Rodenbough et al. (2016); MgO: Rodenbough et al. (2016); CeO_2: Zhang et al. (2002); FeOOH: This study; MnCr2O4: Bhowmik et al. (2006)